

Master Thesis

Coulomb dissociation of ^{26}Ne

Kazuhiro Ishikawa



The Course of Fundamental Physics Graduate School of
Science and Engineering Tokyo Institute of Technology

平成 16 年 2 月 5 日

Abstract

The study of the low-lying $E1$ strength of the neutron-rich ^{26}Ne nucleus was studied by using the Coulomb dissociation. In the unstable nuclei with extreme neutron to proton ratios, low-lying $E1$ strength at very low excitation energy was predicted. For ^{26}Ne , a coherent dipole vibration of the neutron skin against the the core was predicted in theory. The current study aims at observing such an exotic collective excitation. Although the final goal of this study is to derive the $E1$ strength distribution from the relative energy spectrum $^{25}\text{Ne}+n$, we show here the preliminary analysis on the inclusive cross sections and angular distributions for the breakup reaction channels $^{26}\text{Ne}+\text{Pb}\rightarrow^{22-25}\text{Ne}+n+x$, $^{26}\text{Ne}+\text{Al}\rightarrow^{22-25}\text{Ne}+n+x$. This particular study aims at developing a method to distinguish the Coulomb dissociation component from the nuclear breakup.

The experiment was performed at RIKEN Projectile fragment Separator RIPS. The unstable beam of ^{26}Ne was produced by RIPS and bombarded Pb and Al targets to excite and breakup this projectile. The outgoing Ne fragment was detected in coincidence with a neutron.

Breakup cross sections of ^{26}Ne into $^{22-25}\text{Ne}$ with Al and Pb targets were obtained as well as the angular distributions of these fragments. In the analysis, we have observed distributions of two components of angular distribution, so called narrow and wide component. The wide component was explained by the fragmentation model. On the other hand, narrow component and cross sections were not well understood yet. Further analysis and theoretical studies are thus to be done for the near future.

Contents

1	Introduction	3
1.1	Neutron-rich nuclei	3
1.2	Low-lying E1 strength	4
2	Experimental Considerations	8
2.1	Neutron-rich nuclei, ^{26}Ne	8
3	Experimental Setup	14
3.1	Production of ^{26}Ne RI Beam	14
3.1.1	Riken Projectile-Fragment Separator(RIPS)	14
3.1.2	Target	17
3.2	Detector System	17
3.2.1	Incident Beam Detectors	17
3.2.2	Detector for Reaction Products	19
3.2.3	Silicon Strip Detector	19
3.2.4	Gamma-Ray Detectors	21
3.2.5	Neutron Detector	22
3.2.6	Trigger for Data Acquisition	22
3.3	Data Set	23
4	Analysis	25
4.1	Beam line detectors analysis	25
4.1.1	Timing calibration for TDC at Radio Frequency (RF), plas- tic scintillator and PPAC's	25
4.1.2	Particle Identification by using the F2 Plastic Schintillator	26
4.1.3	Particle Identification of incident ^{25}Ne beam	26
4.1.4	Particle Identification of incident ^{26}Ne beam	28
4.2	Purity estimation of the incident beam	28
4.2.1	Determination of the incident beam momentum	30
4.3	Analysis of PPAC	32
4.3.1	Efficiency calculation of PPAC	32
4.4	Particle Identification of Reaction Products	35
4.4.1	Energy Calibration of Silicon Strip Detector	35

4.4.2	Particle Identification of Reaction Products	35
4.4.3	Improving the mass resolution of SSD	36
4.5	Acceptance Correction of SSD	41
5	Result and Discussion	45
5.1	Reaction Cross Section	45
5.2	Angular distributions of Ne fragments	47
6	Conclusion	52
A	Appendix	53
A.1	Coulomb Potential	54
A.2	Analysis PPAC	55
A.3	Analysis of Gamma Rays	57
A.3.1	Energy calibration	57
A.3.2	Timing Gate for Background Reduction	58
A.4	Doppler shift correction	59
A.4.1	Result of the obtained spectrum from Ne isotopes	61
A.4.2	Energy resolution of the Doppler corrected γ -ray spectrum	61
B	Appendix on NaI	68
B.1	Decay Table	68
B.1.1	Decay formula	69
B.2	Efficiency calculation of the DALI	71
C	Cross Section Estimation	73
C.1	formula	73
C.1.1	The list of trigger event and livetime	75
C.1.2	Error estimation of cross section	80
D	Gold Haber Model	83
D.1	Coulomb dissociation from the Cross-section	86
E	Acknowledgements	90

1 Introduction

1.1 Neutron-rich nuclei

Recent development of high-energy heavy-ion accelerators has opened a new era. A large number of radioactive unstable nuclei lying far from the β -stability line is accessible by using new heavy ion accelerators. About six thousand of the radioactive nuclei were theoretically predicted which is huge compared to three hundred stable nuclei. Most of these radioactive nuclei are still to be explored in such a facility.

One of the interesting phenomenon has recently been found for weakly bound neutron-rich nuclei with extreme neutron to proton ratios, such as neutron halo and the skin. In Fig.1.1, the light region of the nuclear chart is shown, where neutron halo nuclei are marked. The halo structures are characterized by a twofold structure composed of a saturated dense core and a neutron halo with lower density extending out of the core as shown in the upper part of Fig.1.1. Such a structure was first indicated by systematic measurements of interaction cross sections for Li isotopes at 800 MeV/u by Tanihata *et al.*[1]. The large interaction cross sections observed for ^{11}Li indicated the extremely large r.m.s radius of 3.10 fm, which is about 20 % larger than that expected for the standard nuclei ($R= 1.2A^{1/3}$ fm). In a subsequent experiment, Kobayashi *et al.*[2] found that the transverse momentum distribution of ^9Li emitted from the fragmentation of ^{11}Li at 800 MeV/u has much narrower width than those for usual nuclei expected by the Goldhaber scaling law[3]. Since the observed momentum width represents the momentum of two valence neutrons of ^{11}Li , these neutrons should extend spatially outside the usual nuclear radius according to the uncertainty principle. In other words, two valence neutrons form a neutron halo surrounding the saturated ^9Li core. Evidences for the halo structure of ^{11}Li are also found from the narrow angular distribution of neutrons emitted in the fragmentation ^{11}Li [4], the narrow longitudinal momentum distribution of emitted ^9Li in the same reaction, and the similarity of the quadrupole moments between ^9Li and ^{11}Li [8].

two neutron halo one neutron halo

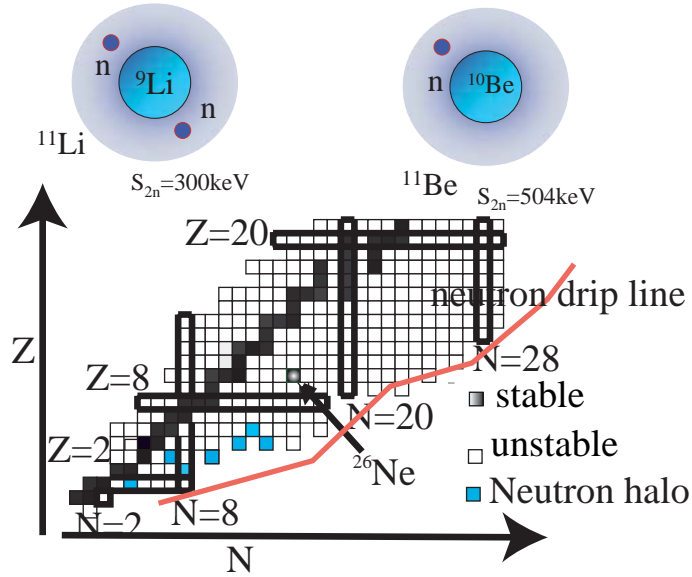


Figure 1.1: Nuclear chart for light nuclei. The neutron-rich nucleus ^{26}Ne is located in the neutron-rich region around $N=20$. The exotic neutron halo is near the neutron drip line. Neutron halo is attributed to the small separation energy which forces the wave function to penetrate out from the range of the potential well by the quantum tunneling effect.

1.2 Low-lying E1 strength

At excitation energies above the particle threshold, the nuclear response of stable nuclei is dominated by collective vibrations of various multiplicities, i.e., giant resonance as listed in Table 1.1. For the instance, the excitation energy for the isovector E1 mode (Giant Dipole Resonance (GDR)) is as high as about 10-20 MeV. However, for the nuclei with neutron halos, appreciable E1 strengths have been observed at much lower excitation energies compared to the usual GDR region. For the one-neutron halo nuclei ^{11}Be [6, 7] and ^{19}C [9], the observed dipole strength at very low excitation energies was interpreted as a quantum-mechanical threshold effect, involving nonresonant transitions of the valence neutron into the continuum instead of the resonances. For ^6He and ^{11}Li , a coherent dipole vibration of the two

spin isospin	multipolarity	I^π	E_x
Isoscalar(T=0)	monopole	0^+	$80A^{-1/3}$
	quadrupole	2^+	$65A^{-1/3}$
	octopole	3^-	$30A^{-1/3}, 120A^{-1/3}$
Isovector(T=1)	monopole	0^+	$60A^{-1/3}$
	dipole	1^-	$31A^{-1/3}+21A^{-1/6}, [80A^{-1/3}]$
	quadrupole	2^+	$130A^{-1/3}$

Table 1.1: The list of the Giant Resonance.[18]

halo neutrons against the core was discussed. The first attempt to interpret the phenomenon addressed a notion of so-called Soft Dipole Resonance(SDR)[17]. This resonance may occur as an oscillation of a core nucleus against the halo neutrons with low frequencies. The excitation energy may be low since the restoring force between the core and valence neutron should be weak due to the low density of valence neutron. This mode is decoupled from the major oscillation mode which occurs between the saturated protons and neutrons in the core. Although the vibrational picture for the SDR was suggested in the theory, the interpretation of the experimental data is still under discussion. Such a mode, in literature sometimes referred as pygmy resonance, may arise if less tightly bound valence neutrons vibrate against the residual core (Fig1.3).

A pioneering work of the low lying GDR has been performed at GSI on the Oxygen isotopes [11]. In this work, the evolution of giant dipole strength with the neutron-rich oxygen isotopes from A=17 to A=22 was measured. For all neutron-rich isotopes investigated, the dipole strength appears to be strongly fragmented with a considerable fraction observed well below the giant dipole resonance, much in contrast to the dipole response of stable nuclei. To which extent the low-lying dipole strength observed in the neutron-rich oxygen isotopes involves coherent excitations or this is due to single particle transitions remain a subject of detailed theoretical study.

In the experiment, we have attempted to search for the SDR of the neutron-rich ^{26}Ne isotope which is located near the drip line as shown in Fig.1.1. The ^{26}Ne was predicted as the candidate of a SDR[26]. It shows that the stable ^{20}Ne has a main peak centered at the GDR energy of 20 MeV in Fig. 1.3. On the other hand, for the neutron-rich isotope ^{26}Ne , the calculation predicts a strong redistribution of the strength, a low energy component appearing clearly at 8 MeV excitation energy, corresponding to a sizeable portion of the energy weighted sum rule in the upper part of Fig. 1.3.

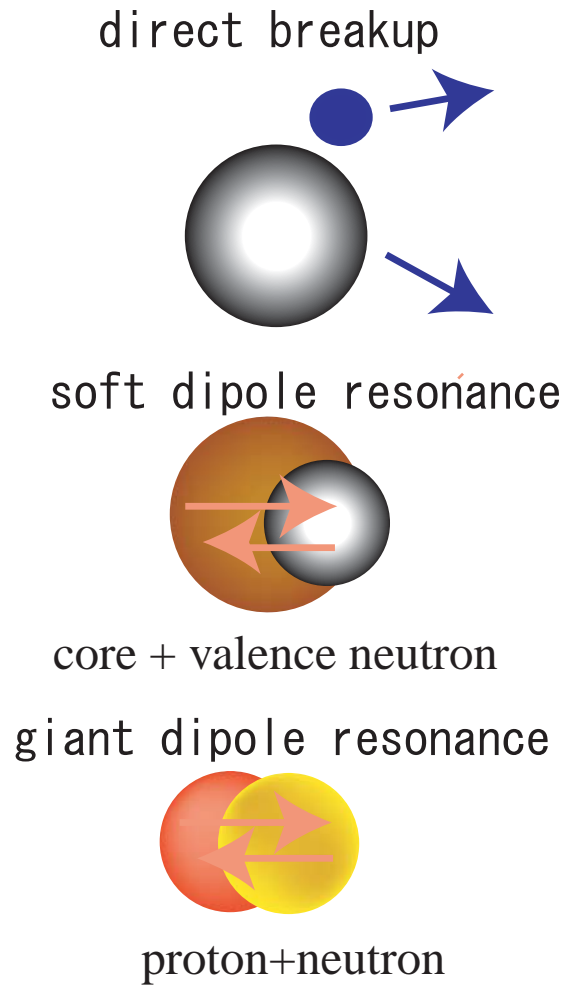


Figure 1.2: The schematic view of the dipole motion. In the dipole breakup, the final states are continuum states instead of a resonant state. In the SDR, the resonance is the oscillation of a core nucleus against the halo neutrons with low frequencies. In the GDR, the resonance is the oscillation between the proton and the neutron.

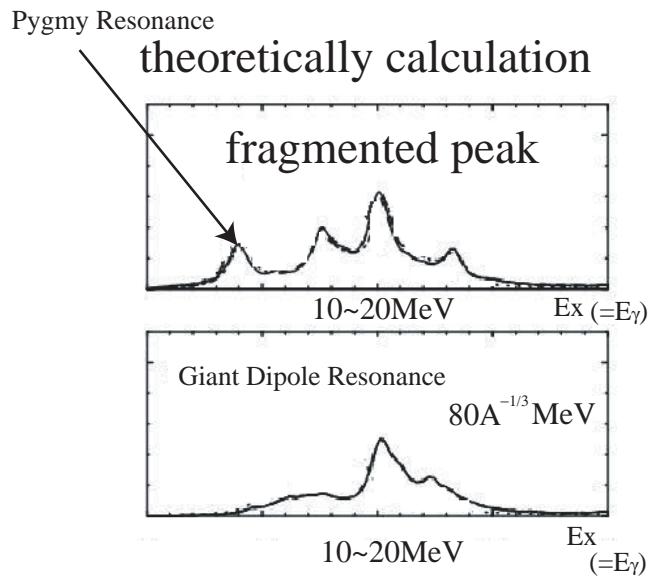
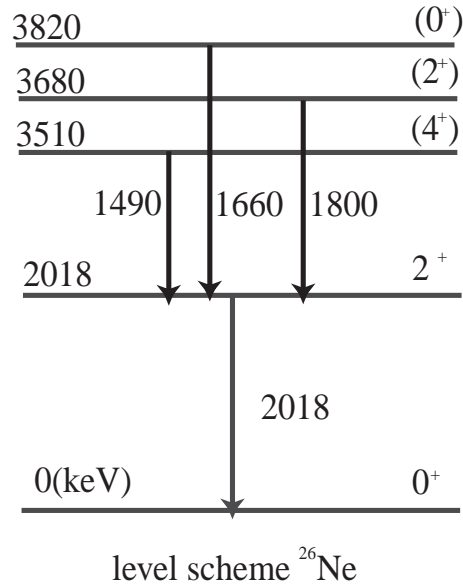


Figure 1.3: The schematic view of the E1 calculation for ^{26}Ne and ^{20}Ne . In ^{20}Ne , the peak of the GDR is centered at about 20 MeV. On the other hand, the peak of GDR for ^{26}Ne is fragmented. In the experiment, We search for the pygmy resonance about 8 MeV.

2 Experimental Considerations

2.1 Neutron-rich nuclei, ^{26}Ne

The radius of ^{26}Ne is known to be 2.86 fm(r.m.s).[22]. The one neutron separation energy and two neutron separation energy is 5.6 MeV and 9.8 MeV, respectively. The excitation energies and spin assignments for the low lying states are illustrated in Fig. 2.1. Some calculations for the isovector giant dipole resonance strength predicts a strong redistribution of the strength, a low energy component appearing clearly at about 8 MeV[26].



Coulomb excitation reaction serves as one of the powerful spectroscopic tools for investigating excited states of nuclei. An appealing feature of this reaction is the clear understanding of its reaction mechanism. In the classical Coulomb excitation experiment, the incident energy is usually set below the Coulomb barrier in order to avoid the influence of excitations via a strong interaction.

In this experiment, the energy of the incident beam is 58 MeV/u. The relative energy is the following.

$$E_{\text{rel}} \simeq 1400 \text{ MeV (Pb)}$$

The present works, nevertheless, utilized a ^{26}Ne beam with the intermediate incident energy of 58 MeV/u, which lies far above the Coulomb barrier of 170 MeV (see Appendix A.1). The reason to use higher incident energy is that the reaction yield is much higher, which is important in the experiment using a secondary beam whose intensity is generally weak. The high reaction yield is due primarily to the large cross section of the Coulomb excitation, which often dominates over other reaction channels and almost eliminates the ambiguity caused by the contribution from the nuclear reaction. The large cross section is attributed to the long range nature of the Coulomb interaction, having a dependence of $\sim 1/r^{(\lambda+1)}$ for the λ -th multipolarity. As shown in Fig. 2.2, at the intermediate incident energies, the cross sections are relatively large even for $E_x=5$ MeV. In applying Coulomb excitation to unstable nuclei, it is practical to employ the radioactive nuclei provided as a beam. Hence, a projectile is to be excited by a Coulomb field of a high-Z target. The basic phenomenon of Coulomb excitation in the intermediate and high incident energy domains is shown in Fig. 2.1. As seen in the figure, a Lorentz-contracted electric field acts on a projectile nucleus when the projectile passes fast by a high-Z target at an impact parameter b . In this electric field, the incident nucleus absorbs a virtual photon 2.4. Hence, Coulomb excitation can be expressed as a photo-absorption process induced by a virtual photon, as schematically represented in Fig. 2.1 (b). This picture is treated by the so-called the equivalent-photon method [19, 20]. In this method, Coulomb excitation cross section at excitation energy E_x is expressed simply as a product of photo-absorption cross section $\sigma_\gamma^{E\lambda}(E_x)$ and virtual photon number $N_{E\lambda}(E_x)$ which is obtained by integrating $N_{E\lambda}(E_x, b)$ (photon flux at a impact parameter b) from the cutoff impact parameter b_0 to infinity, i.e.,

$$\frac{d\sigma_c(E_x)}{dE_x} = \int_{b_0}^{\infty} 2\pi b db \frac{N_{E\lambda}(E_x, b)}{E_x} \sigma_\gamma^{E\lambda}(E_x) \quad (2.1)$$

$$= \frac{N_{E\lambda}(E_x)}{E_x} \sigma_\gamma^{E\lambda}(E_x) \quad (2.2)$$

where λ represents a multipolarity of the transition. The photo-absorption cross section is related to the reduced transition probability.

$$\sigma_\gamma^{E\lambda}(E_x) = \frac{(2\pi)^3 (\lambda + 1)}{\lambda [(2\lambda + 1)!!]^2} \left(\frac{E_x}{\hbar c}\right)^{2\lambda-1} \frac{dB(E\lambda)}{dE_x} \quad (2.3)$$

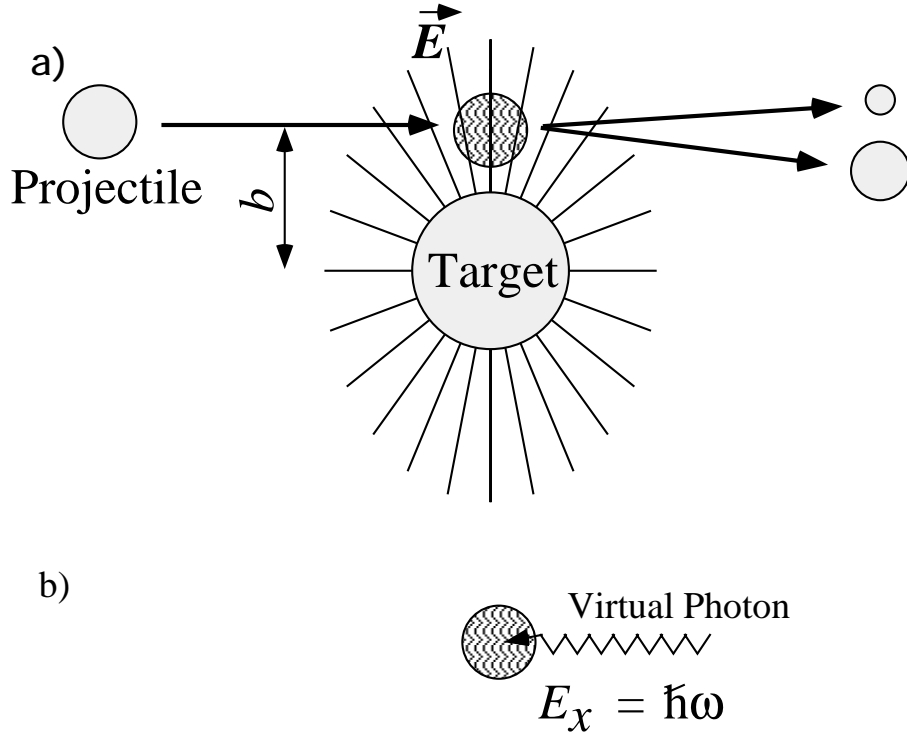


Figure 2.1: a) Schematic drawing for Coulomb excitation process. An electric field \vec{E} , illustrated by lines of electric force, is provided in the projectile rest frame, and thus is Lorentz-contracted in the beam direction. The final state is depicted as a dissociated state (Coulomb dissociation). b) The electric field from the target is interpreted as a virtual photon flux (equivalent photon method). The absorption of one photon in the typical direction is illustrated.

Depending on the succeeding decay process, Coulomb excitation cross sections can be measured in different ways. The decay processes are categorized as follows: 1) If the excitation energy is above a particle-decay threshold, the excited state will pre dominantly decay by a particle emission (Coulomb dissociation). 2) If the excitation energy is below any of particle thresholds, the excited state will decay by a γ -ray emission. In the case of 1) further γ -ray emission follows when the decay product is in bound excited states. In Fig. 2.3, such excitation and decay schemes are shown for ^{26}Ne . The main part of the present work employed the breakup case, where the cross section was determined by measuring the dissociation cross section.(Case 1) We also independently studied Coulomb excitation of ^{26}Ne to the bound state. The $B(E2)$ of this transition by using Coulomb exaltation was previously measured at MSU[12], so that we can use this excitation as a reference.(Case 2)

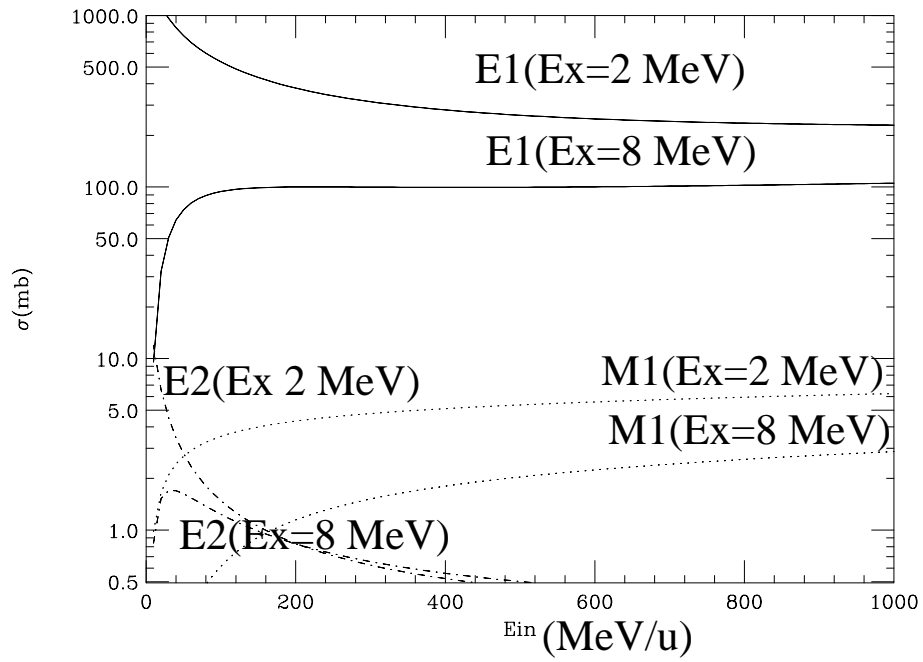


Figure 2.2: Electromagnetic(Coulomb) excitation cross section of E1, M1 and E2 transitions of ^{26}Ne as a function of incident energy. These curves are calculated by the equivalent photon method.

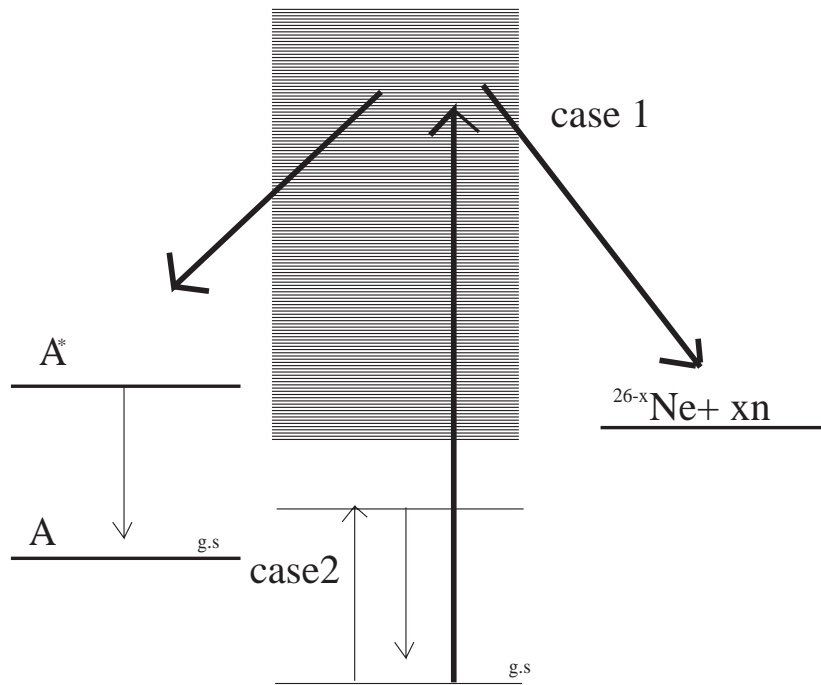


Figure 2.3: Decay schemes for the Coulomb excitation and for searching for the new bound excited states.

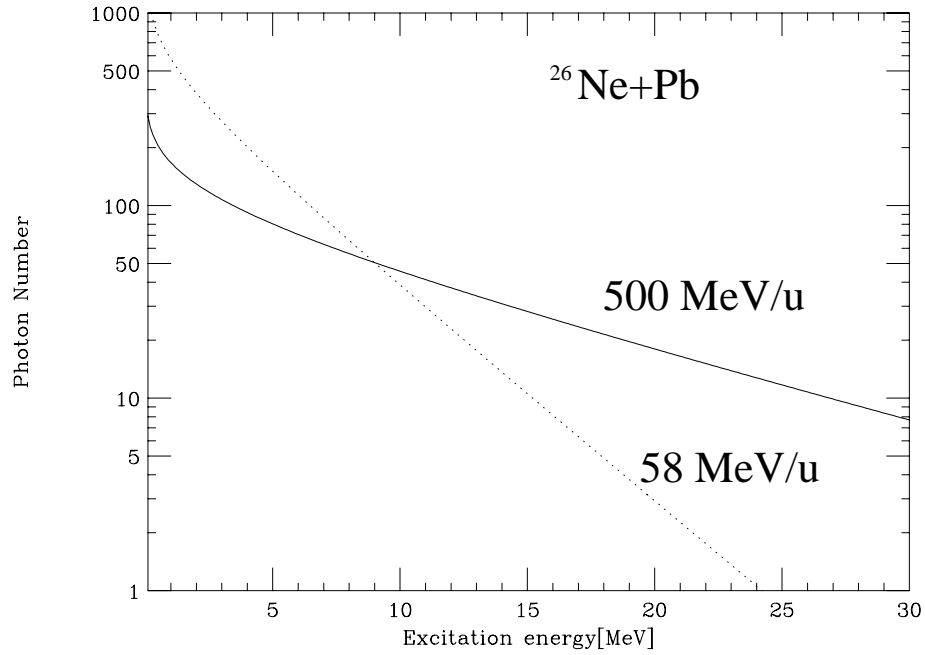


Figure 2.4: Virtual photon spectrum $N_{E1}(E_x)$, estimated for the ^{26}Ne projectile with 58 MeV/nucleon and 500 MeV/nucleon, respectively on a Pb target. The spectrum is represented regarding the Coulomb excitation above the threshold energy ($E_x=5.6\text{MeV}$). Note that the photon numbers decreases with E_x and the decrease is slow with the energy of the incident beam.

3 Experimental Setup

3.1 Production of ^{26}Ne RI Beam

The experiment was performed at RIKEN Projectile-fragment Separator RIPS [13]. Schematic views of RARF and RIPS are shown in Figs 3.1 and 3.2, respectively. The primary beam of ^{40}Ar at 95 MeV/nucleon bombarded a 2-mm-thick Be target and various isotopes were produced by the projectile fragmentation reaction in Fig D.1. The secondary beam of ^{26}Ne was collected and analyzed by RIPS. The average intensity and purity of the ^{26}Ne beam were about 6 kcps and 80%, respectively, with 58 MeV/nucleon just before the reaction target.

3.1.1 Riken Projectile-Fragment Separator(RIPS)

A separation of isotopes was performed by using two dipole magnets(D1-D2) and an Al degrader(F1). In the magnetic field, a charged particle follows Lorentz force in Eq.3.1.

$$B\rho \propto \frac{A}{Z} \quad (3.1)$$

where

- B : magnetic field strength
- ρ : radius of curvature
- Z : atomic number
- A : mass number

This shows that the particle is spatially separated by A/Z , which facilitates a separation of isotopes in the D1 dipole magnet section of RIPS. The energy loss of a charged particle passing through a matter is given by the following.

$$\Delta E \propto \frac{Z^2}{v^2} = Z^2 \text{TOF}^2 \quad (3.2)$$

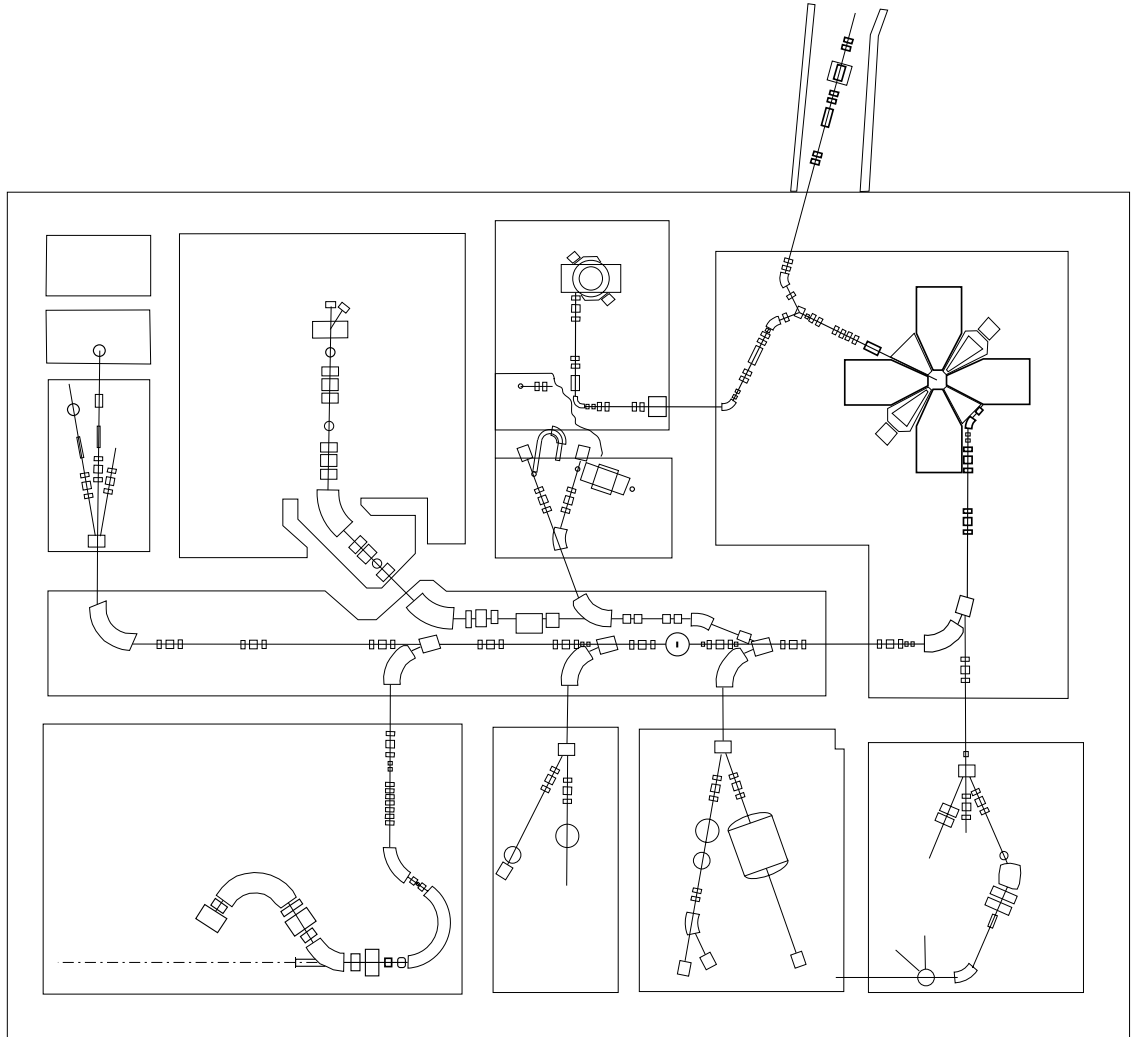


Figure 3.1: Layout of the RIKEN Accelerator Research Facility (RARF). An ^{40}Ar beam was pre-accelerated with the AVF Cyclotron and was mainly accelerated up to 95 MeV/nucleon with the Ring Cyclotron. The beam is transported through the beam transport line in the room D onto the production target at RIPS. The fragment separator RIPS [13] lies in the room D and E6.

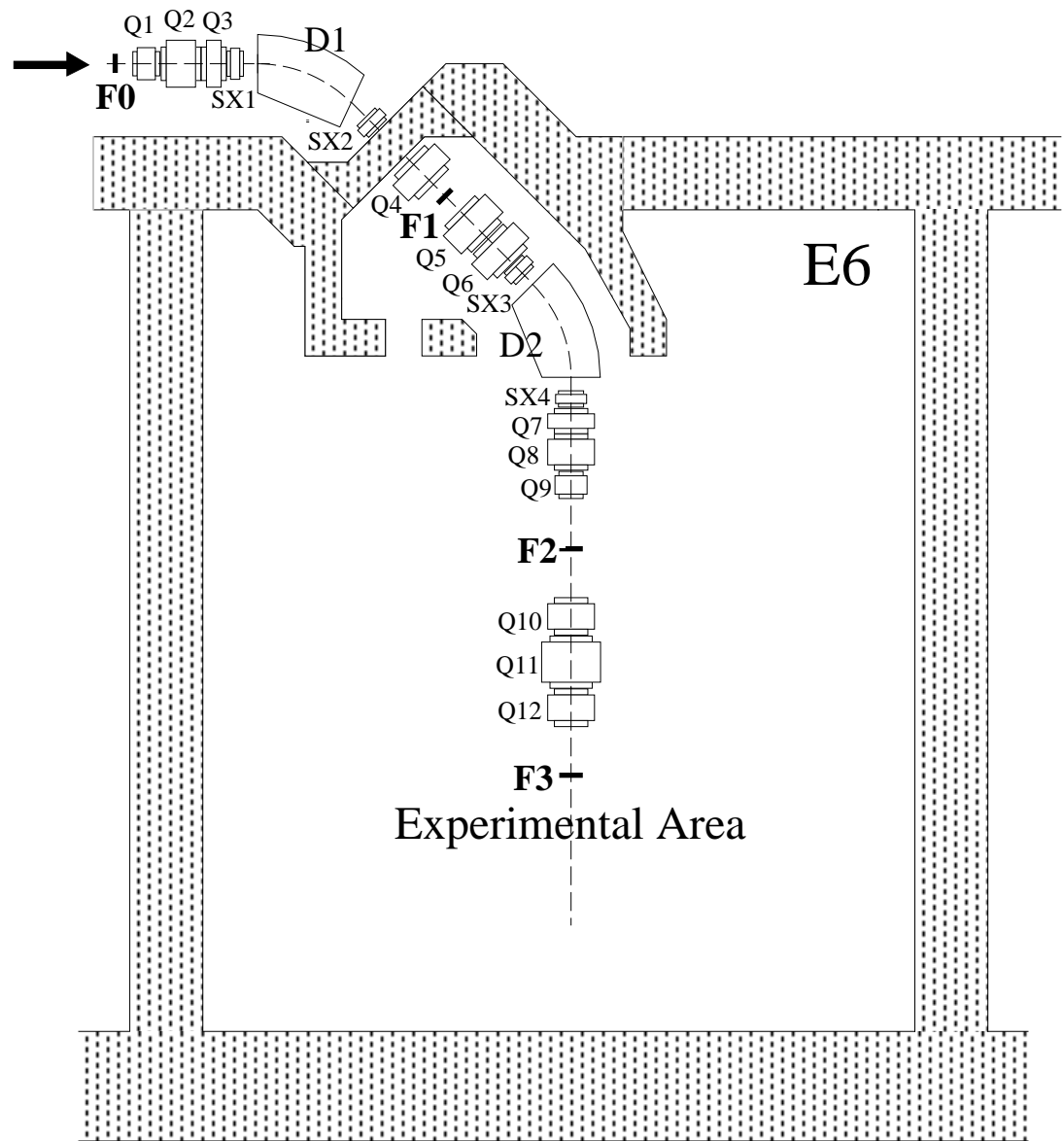


Figure 3.2: Layout of the radioactive beam line RIPS. The separation of the secondary beam is achieved in two stages: F0-F1 and F1-F2. The F3 focus was used to locate the secondary target.

where

- ΔE : energy loss of a charged particle
- v : velocity
- TOF: time of flight

A Charged particles passing through a matter can be separated by the Z number Eq. 3.2. By the different amount of the energy loss at F1, different isotopes may have different $B\rho$ values after F1, which facilitates a separation of isotopes in the D2 dipole magnet section of RIPS. Therefore, the selection of A/Z was performed by D1 magnet and the selection of Z was performed by an Al degrader located at F1. The incident particle was analyzed by the second dipole magnet (D2) through the $B\rho$.

3.1.2 Target

In the experiment, a natural Pb target with 0.23 g/cm^2 thickness for the Coulomb dissociation reaction and a natural Al target with 0.13 g/cm^2 for the evaluation of the nuclear breakup contributions were used, respectively. Runs with no target placed in the target frame (labelled 'empty') were also performed in order to subtract the background events caused by reactions with materials other than the target.

3.2 Detector System

This section is the description of the detectors which was used in this experiment and the schematic views of the setup is shown Fig.3.3.

3.2.1 Incident Beam Detectors

Incident beam detectors were constituted by the plastic scintillator at F2 (F2PL) and a set of two parallel-plate avalanche counters (PPAC's) [14] placed at F3 (F3PPAC-A, F3PPAC-B). The schematic view of the F2 plastic scintillator and PPAC is shown in Fig. 3.4 and 3.5, respectively.

The purpose of the F2PL is the identification of the incident particles and the measurement of the velocity of the incident particles. The identification of the incident particles was performed by the TOF- ΔE method (see Eq. 3.2). The plastic scintillator was 0.5 mm thickness. The scintillation light was read out from both left and right ends of the detector by photo-multiplier tubes.

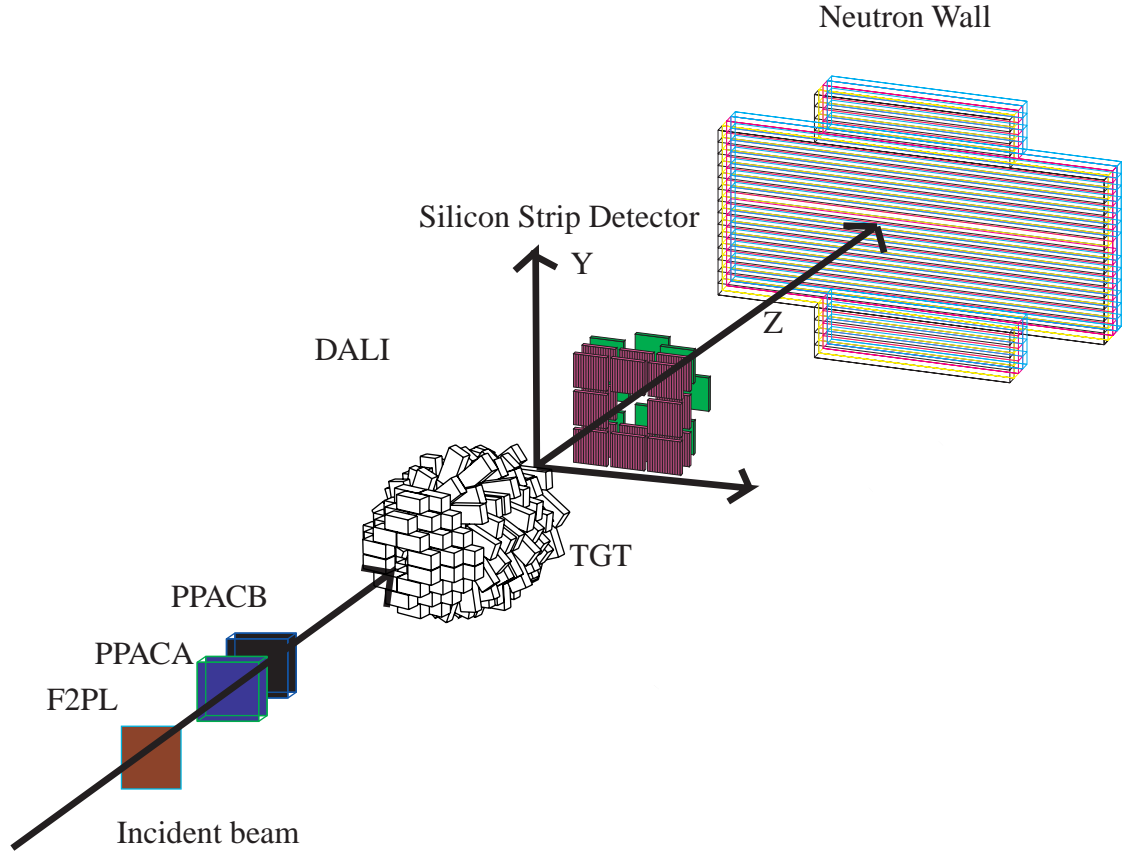


Figure 3.3: Schematic view of the setup backward F3. The detectors system comprises 152 NAI(Tl) detectors for detecting γ -rays, $\Delta E - E$ Silicon Strip Detector for detecting outgoing reaction products, and Neutron Wall for detecting neutrons produced in the reaction.

The incident angle of the beam was measured by two PPAC's. The incident momentum vector of the beam was measured by using both from F2PL and the incident angle from PPAC's. These two PPAC's were 30 cm apart from each other along the beam axis. Delay-line-type PPAC's were used in this experiment [14]. The active area of the PPAC was $100 \text{ mm} \times 100 \text{ mm}$. PPAC was composed of one anode plate, and two cathode plates which were strip type. From both side signals on the strip, incident position of the beam can be read.

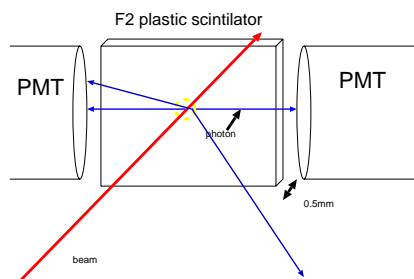


Figure 3.4: Schematic view of the F2 plastic scintillator.

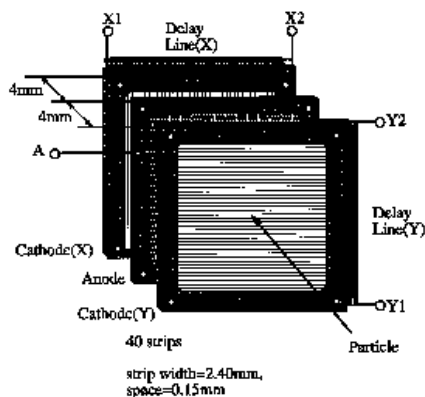


Figure 3.5: picture of the PPAC

3.2.2 Detector for Reaction Products

This section is the description of the detectors which is placed backward F3, and the schematic view of the detectors is shown in Fig.3.6.

3.2.3 Silicon Strip Detector

Identification of the reaction products was necessary for reaction channel selection, since a large variety of isotopes were produced in the secondary fragmentation reaction. In this experiment, particle identification of the fragments was performed by using four-layer Si strip detectors (SSD) composed of ΔE and E counters located at about 1.2 m downstream of the target. ΔE stands for the energy deposit in the first two layers of the silicon telescopes, and E denotes the sum of the energy deposit in the second two layers of the silicon telescopes. Figure 3.7 shows a schematic view of the silicon detector telescope. The first two layers were composed of eight Si detectors which were used for position detection. The posi-

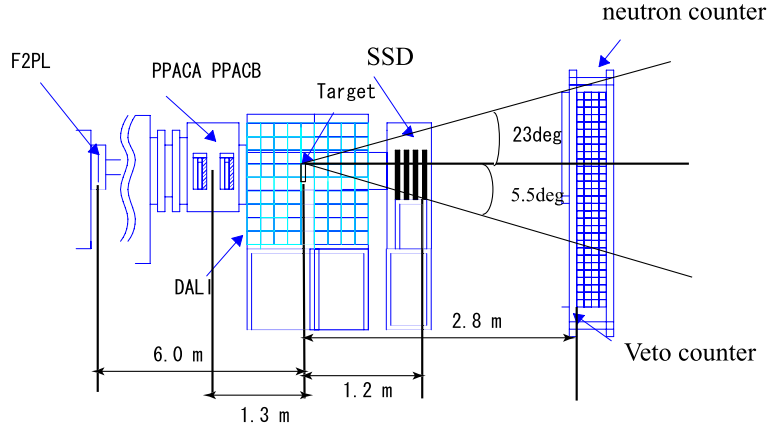


Figure 3.6: Schematic view of the setup backward F3.

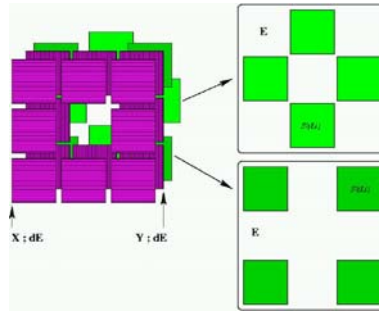


Figure 3.7: The Schematic view of SSD. Left:particle identification of the fragments was performed by using four-layer Si strip detectors (SSD) composed of ΔE and E counters located at about 1.2 m downstream of the target.

tion and intrinsic energy resolution of ΔE counters were 5 mm and 2% (FWHM), respectively. The last two layers were the E counter composed of eight Si(Li) detectors with 3 mm thickness, and an intrinsic energy resolution of 3% (FWHM). In non-relativistic kinematics, the kinetic energy of a particle can be expressed in terms of the mass number A and the TOF as follows.

$$E = \frac{1}{2}Av^2 \propto \frac{A}{\text{TOF}^2} \quad (3.3)$$

From Eq. 3.2 and Eq. 3.3,

$$E\Delta E \propto AZ^2 \quad (3.4)$$

Therefore, by the $E\Delta E$, the particle identification of the fragments can be measured.

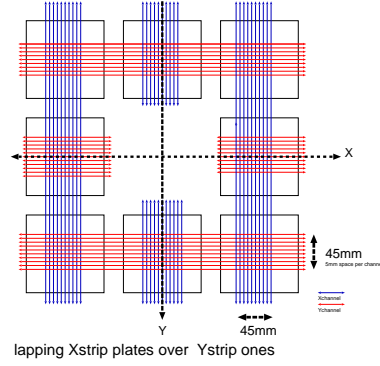


Figure 3.8: readout position of SSD. Red line was for X strip at the first layer. Blue line was for Y strip at the second layer. The position of the reaction products was measured by the signal from both X and Y strips.

The position of the fragments was performed by using the strip (see in Fig. 3.8). This position resolution is 5 mm. The momentum of the fragments was analyzed from the E of SSD. Thus, the momentum vector of the fragments was calculated by using both the angle of the fragments from the position of fragments and from the momentum of it. The angle of the reaction products in the laboratory frame was determined by the position information both PPAC and SSD. \mathbf{P}_{in} was measured by the F2PL and PPAC. \mathbf{P}_{out} was measured by the SSD.

$$\theta = \arccos \frac{\mathbf{P}_{in} \cdot \mathbf{P}_{out}}{|\mathbf{P}_{in}| |\mathbf{P}_{out}|} \quad (3.5)$$

3.2.4 Gamma-Ray Detectors

An array of 152 NaI(Tl) scintillation detectors (DALI2) was placed around the target to detect γ rays emitted from the excited fragments in flight ($v/c \sim 0.3$). The schematic view is in Fig. 3.9. The high granularity of DALI2 allowed us to measure the angle of the γ -ray emission. The angular information was used to correct for the large Doppler shift, which was caused by a moving reaction products emitting γ rays in a high velocity ($v/c \sim 0.3$). For 2 MeV γ -rays, the efficiency was calculated to be around 13% (see in Appendix B.2) with an intrinsic energy resolution of 7% (FWHM).

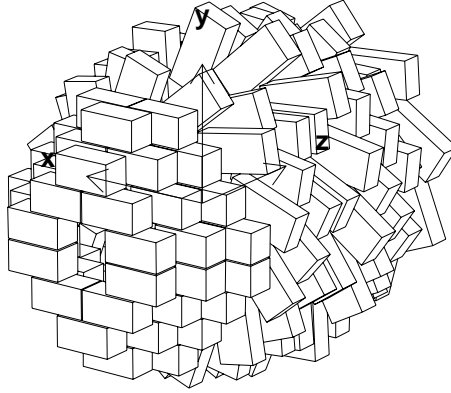


Figure 3.9: Schematic view of 152 NaI(Tl) scintillation detectors (DALI2).

3.2.5 Neutron Detector

The neutrons produced in the reaction were detected by the neutron wall (see in Fig. 3.10). The neutron wall located 3 m downstream of the target was composed of 4 layers. Each layer had 29 plastic scintillators. The 28 veto counters were installed in front of the neutron counter. The veto counter rejected events in which a charged particle hits in the neutron wall. Two photo-multipliers, coupled to both ends of each scintillator in the horizontal direction, read out light-outputs of the scintillator. The average of the two PMT timings was used to define the neutron TOF between the target and NEUT. The timing difference between PMT's determined the neutron hit position in the horizontal direction. The vertical position was distinguished by identifying the rod.

3.2.6 Trigger for Data Acquisition

The data for the present experiment were stored event-by-event, using a data acquisition system. We took particular care of reducing the dead time in data acquisition and the contribution from background events mainly caused by the incident beam with no reactions in the target. Therefore combinations of the following conditions were imposed.

- *DSBEAM*: the signal generated once each five hundred *BEAM* signals
- $BEAM \otimes SSD \otimes NEUT$: a logical *AND* of the trigger logic *BEAM* and *SSD* and *NEUT*
- $BEAM \otimes SSD \otimes DALI$: a logical *AND* of the trigger logic *BEAM* and *SSD* and *GAMMA*

Neutron wall

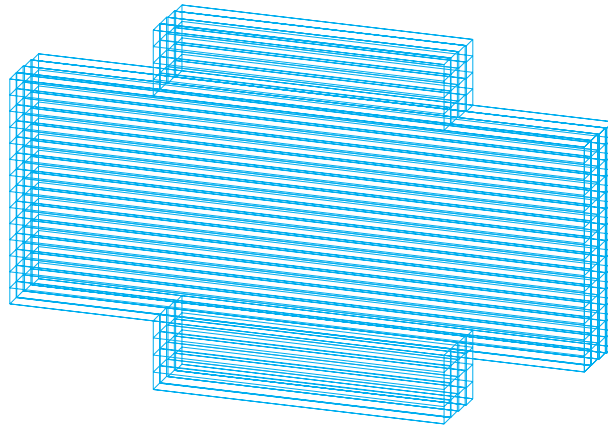


Figure 3.10: The schematic view of Neutron Wall(NEUT))

Figure 3.11 shows a trigger logic diagram employed in the present experiment. The *DSBEAM* was used to monitor the beam profile during the experiment.

3.3 Data Set

Table 3.1 shows a list of experimental data set taken in the present experiment. The data are categorized into those for the calibration runs and those for extracting the spectra of interests. Calibration runs of ^{25}Ne were performed to measure the absolute energy of SSD. Calibration runs of proton and deuteron runs were performed to measure the absolute energy of NEUT. Calibration runs of ^{25}Ne brass which produced large number of γ rays were performed to measure the absolute timings of NEUT. The experimental runs aiming at obtaining the interesting spectra were performed using three different target, Pb, Al, empty (see the section of target).

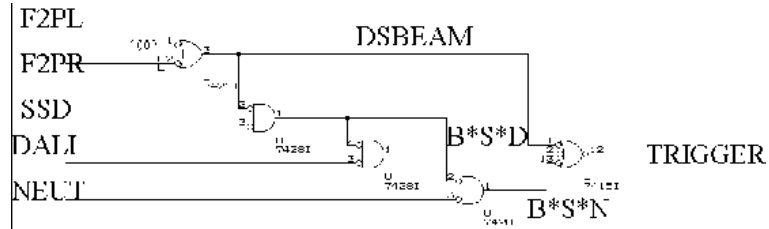


Figure 3.11: Circuit diagram for trigger signal of data acquisition system.

Secondary Beam	Target	Trigger
^{26}Ne (58 MeV)	Pb	<i>COIN</i> or <i>DSBEAM</i>
^{26}Ne (58 MeV)	Al	<i>COIN</i> or <i>DSBEAM</i>
^{26}Ne (58 MeV)	empty	<i>COIN</i> or <i>DSBEAM</i>
^{26}Ne for gamma products	Brass	<i>COIN</i> or <i>DSBEAM</i>
^{25}Ne (60, 55, and 50 MeV) for SSD	Pb	<i>COIN</i> or <i>DSBEAM</i>
proton (70, 50, 40 MeV) and triton (87 MeV) for neutron counter	Pb	<i>COIN</i> or <i>DSBEAM</i>
proton (30 MeV) for Veto counter	empty	<i>COIN</i> or <i>DSBEAM</i>

Table 3.1: *COIN* is the trigger of $(\text{BEAM} \otimes \text{SSD} \otimes \text{NEUT}) \oplus (\text{BEAM} \otimes \text{SSD} \otimes \text{GAMMA})$.

4 Analysis

4.1 Beam line detectors analysis

4.1.1 Timing calibration for TDC at Radio Frequency (RF), plastic scintillator and PPAC's

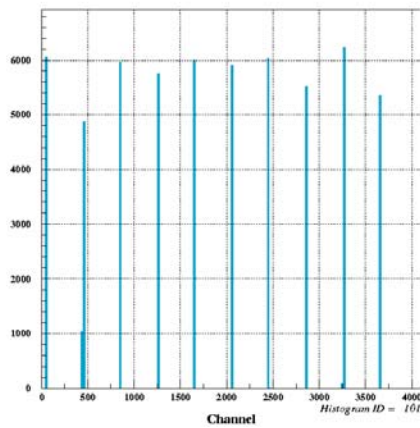


Figure 4.1: Plot of channel versus timing in ns. This calibration was fitted by a linear function of the timing.

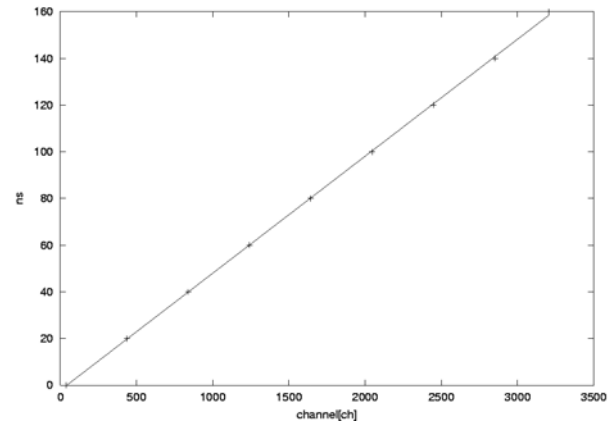


Figure 4.2: TDC pulse Histogram. Histogram obtained using the time calibrator module.

In order to extract physical information from the obtained data, digital data taken by the data acquisition system have to be converted to the physical quantities. For this purpose, we took calibration data, which were clearly related to the corresponding physical quantities. In this subsection, timing signal of RF, plastic scintillator and PPAC's were calibrated by using a time calibrator module. This module generated a start signals followed by a stop signal, and timing of the stop signal with respect to the start signal was changed directly and periodically with a given interval. To convert the obtained digital data to ns, the following function was used (Eq. 4.1). The figure 4.1 and 4.2 show 20 ns pulse plot in the TDC channel and the result of the calibration of timing, respectively.

$$T(\text{ns}) = c_1 X(\text{ch}) + c_2 \quad (4.1)$$

4.1.2 Particle Identification by using the F2 Plastic Scintillator

In this subsection, particle identification of ^{25}Ne run and ^{26}Ne run, is described. The desirable incident beam including other particle which was unable to be rejected at RIPS was able to be selected by using F2PL. Particle identification was performed by using TOF between F0 to F2 versus ΔE at F2PL (see in Eq. 3.2). To compare the obtained data at F2PL with the data from yield estimation code **INTENSITY**[15], particle identification was performed.

4.1.3 Particle Identification of incident ^{25}Ne beam

In the incident ^{25}Ne beam, the estimation of the yield estimation was shown in table. reftab:25Ne, and the obtained data from experiment was shown in Fig. 4.3 and Fig. 4.4. The ^{25}Ne beam can be identified by using these three result.

Fragment	Rate (nucleon/sec)	TOF(F0-F2) (ns)
^{25}Ne	6.2×10^3	201.4
^{26}Na	6.8×10^3	191.1
^{27}Na	9.0×10^3	197.4
^{28}Mg	5.0×10^3	189.0
^{29}Mg	9.8×10^3	194.8

Table 4.1: The result of the estimation of both intensity and TOF(F0-F2) by using **INTENSITY CODE** for ^{25}Ne incident beam. This fragment was produced by the primary beam ^{40}Ar with 95 MeV .

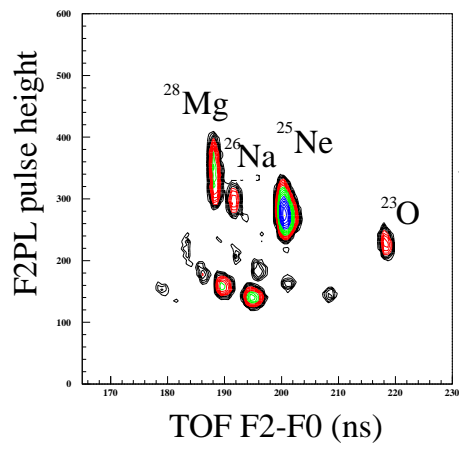


Figure 4.3: TOF versus ΔE from experimental data at ^{25}Ne incident beam

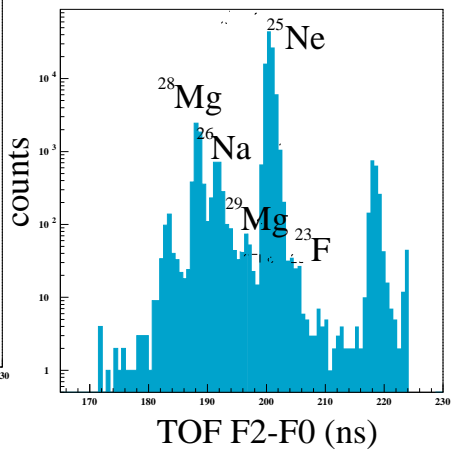


Figure 4.4: TOF spectrum of the incident beam at ^{25}Ne incident beam.

4.1.4 Particle Identification of incident ^{26}Ne beam

In the incident ^{26}Ne beam, the procedure of the identification was same as in the case of ^{25}Ne . As a result, the estimation of the fragment and the obtained data from experiment was shown in Table.4.2, Fig.4.5 and Fig.4.6 respectively.

Fragment	Rate (nucleon/sec)	TOF(F0-F2) (ns)
^{25}Ne	6.2^3	201.4
^{26}Na	6.8^3	191.1
^{27}Na	9.0^3	197.4
^{28}Mg	5.0^3	189.0
^{29}Mg	9.8^3	194.8

Table 4.2: The result of the estimation of both intensity and TOF(F0-F2) by using INTENSITY CODE for ^{26}Ne incident beam. This fragment was produced by the primary beam ^{40}Ar with 95 MeV .

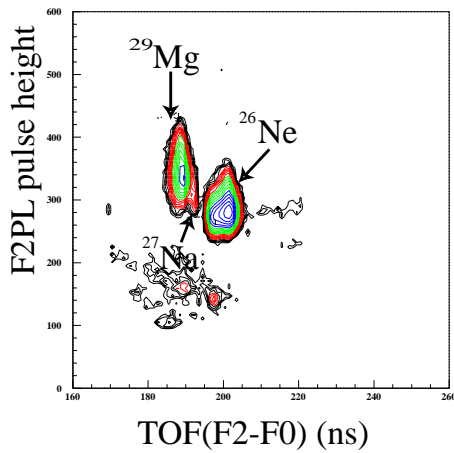


Figure 4.5: TOF versus ΔE from experimental data at ^{26}Ne incident beam.

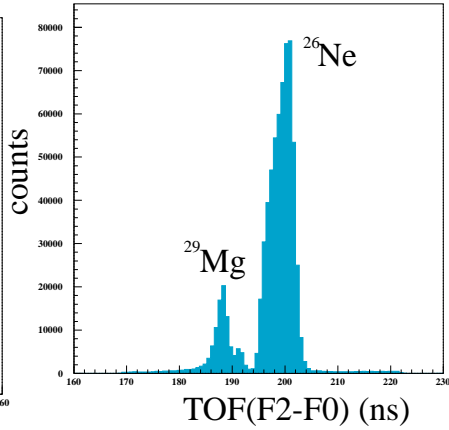


Figure 4.6: TOF spectrum of the incident beam from experimental data at ^{26}Ne incident beam.

4.2 Purity estimation of the incident beam

The purity of ^{25}Ne , ^{26}Ne at F2PL was estimated. The definition of the purity is the following equation.

$$purity = \frac{N_{des}}{N_{total}} \quad (4.2)$$

where

- N_{des} : number of the desired particle
- N_{total} : total number of the incident beam

The purity of ^{25}Ne and ^{26}Ne is the following.

$$\text{purity} = \frac{N_{^{25}\text{Ne}}}{N_{\text{total}}} = 79.6\%$$

$$\text{purity} = \frac{N_{^{26}\text{Ne}}}{N_{\text{total}}} = 77.3\%$$

4.2.1 Determination of the incident beam momentum

From the momentum of the incident beam at D2 by using the magnetic field strength in NMR, the incident momentum of the beam in front of the target taking account of the energy loss passing through the material was calculated. In this analysis, the momentum of the incident beam was approximated by the function in Eq.4.3.

$$P_{\text{aftermaterial}} = C_4 + C_5 P_{\text{beforematerial}} + C_6 P_{\text{beforematerial}}^2 \quad (4.3)$$

- $P_{\text{beforematerial}}$: momentum
- $P_{\text{aftermaterial}}$: momentum corrected

The table.4.3 shows the result of the incident β and momentum between the obtained data calibrated by approximation and the estimation calculated by using the Bethe-Broch equation. Figure.4.7 shows the momentum distribution in front of the target which is calibrated above the procedure. This non-symmetric shape was caused by the acceptance of the RIPS.

	calculation	exp
β_{D2}	0.3427	0.3425
P_{aftertgt}/A	316.75[MeV]	316.70[MeV]
β_{aftertgt}	0.32194	0.3220
E_{aftertgt}/A	52.3803[MeV]	52.41[MeV]

Table 4.3: The comparison the experimental data corrected energy loss with the energy loss calculation. The experimental data was almost same as the calculation data.

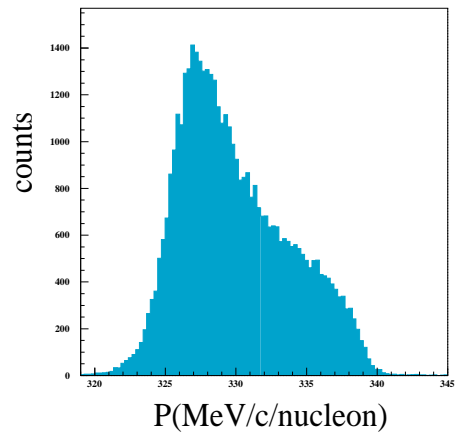


Figure 4.7: the momentum distribution of the incident beam, ^{26}Ne in front of the target.

4.3 Analysis of PPAC

4.3.1 Efficiency calculation of PPAC

In the single hit event of a PPAC, the sum of the both side timing, (T_1+T_2) is constant. By using this feature, we set a gate to (T_1+T_2) for each cathode of all the PPAC's to exclude multi-hit events. The table of result in efficiency and typical histograms are shown in Table. 4.4, and Fig. 4.8, respectively. Incident angle of the beam at the target was made by extrapolation of the position information obtained by two PPAC'(see in appendix.A.2). The obtained spectrum of the incident angle is in Fig. 4.9. By using this angle, the result of the profile of beam size and and momentum vector of the incident beam ^{26}Ne in front of the target can be calculated. Figure. 4.10 and 4.11 are the result of these , respectively.

$$(T_{\text{left}} + T_{\text{right}}) = \frac{X}{V} + \frac{L - X}{V} = L/V \propto \text{constant} \quad (4.4)$$

$$\text{efficiency(PPAC)} = \frac{{}^{26}\text{Ne}_{\text{F2PL}} \otimes (T_{\text{right}} + T_{\text{left}} = \text{constant})}{{}^{26}\text{Ne}_{\text{F2PL}}}$$

efficiency	
PPACa	96.9%
PPACb	96.1%
PPACa \otimes PPACb	93.4%

Table 4.4: The table of efficiency in the two PPAC'S (PPAC-A,PPAC-B)

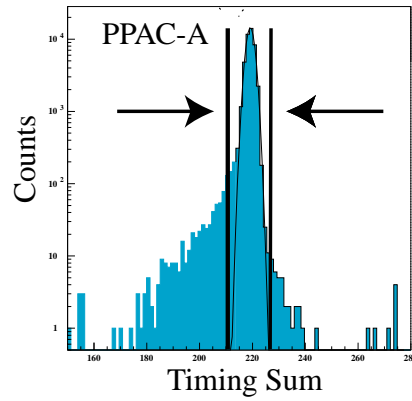


Figure 4.8: Spectra of the sum of timing (T_1+T_2) of both electrodes attached to a PPAC. Single hit events constitute a sharp peak, while multi hit events exhibit smaller (T_1+T_2). The single hit events are selected by the gates indicated by the arrows in the spectra.

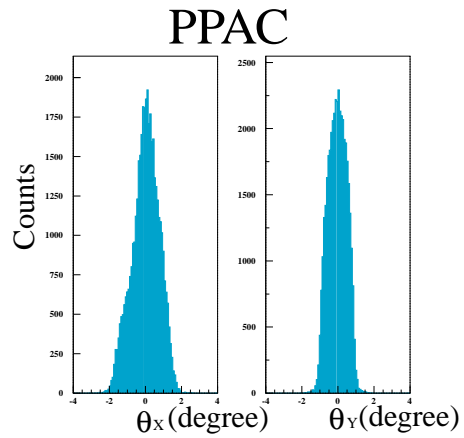


Figure 4.9: θ at target. The plot was made by extrapolation of the position information obtained by two PPAC's before the target.

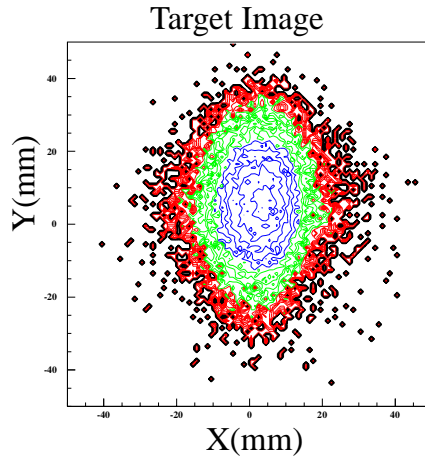


Figure 4.10: Beam spot size of ^{26}Ne . The plot was made by extrapolation of the position information obtained by two PPAC's in front of the target.

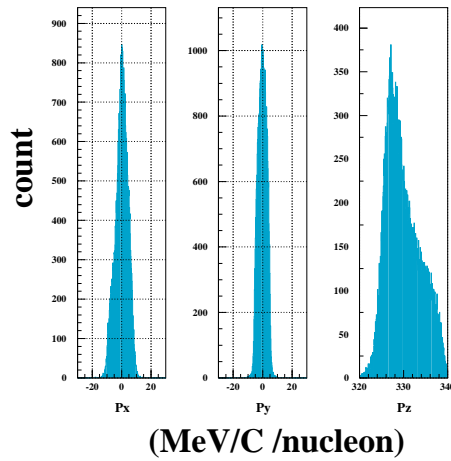


Figure 4.11: momentum vector of the incident beam. Momentum information was obtained by F2PL.

4.4 Particle Identification of Reaction Products

4.4.1 Energy Calibration of Silicon Strip Detector

ΔE_{total} is the energy which is the total energy of the first layer and the second layer.

$$\Delta E_{\text{total}} = \Delta E_{X\text{back}} + \Delta E_{Y\text{back}} \quad (4.5)$$

The reaction products are stopped in the third layer or the fourth layer. The total kinetic energy, E_{total} of the reaction products is the total energy of all SSD layer in case of stopping the reaction products.

$$E_{\text{total}} = \Delta E_{\text{total}} + E \quad (4.6)$$

where

- ΔE_{total} : total energy of ΔE counters
- $\Delta E_{X\text{back}}$, $\Delta E_{Y\text{back}}$: energy loss of the first layer and the second layer, respectively
- E : energy of E counter
- E_{total} : total energy of reaction products

The Energy calibration of the four-layer-Si strip detectors (SSD) was performed by using the ^{25}Ne beams with 60 MeV/A, 55 MeV/A, and 50 MeV/A respectively. Table. 4.5 shows the result of the calibration.

To convert the obtained digital data to energy, the following function was used.

$$E(\text{MeV}) = C_1 X(\text{ch}) + C_2 \quad (4.7)$$

4.4.2 Particle Identification of Reaction Products

Figure. 4.12 shows the ΔE - E correlation of the reaction products from ^{26}Ne incident beam at 58.7MeV/nucleon.

In this analysis, in order to identify clearly the reaction products, E_{total} was redefined.

table of calibration ^{25}Ne beam[MeV/A]				
E_{D2}	ΔE_{total}	deviation	E_{total}	deviation
60.04 MeV/A(cal)	10.16		50.0	
(exp)	10.03	-0.13	49.3	-0.7
55.41 MeV/A (cal)	11.19		43.91	
(exp)	11.20	-0.01	43.96	0.05
49.55 MeV/A (cal)	13.48		36.81	
(exp)	13.51	0.03	36.83	-0.02

Table 4.5: The result of ADC calibration obtained for the silicon detector telescopes with the ^{25}Ne beams with 60 MeV/A, 55 MeV/A, and 50 MeV/A respectively.

$$\dot{E}_{\text{total}} = E + \frac{1}{2}\Delta E \quad (4.8)$$

The equation 4.8 shows that the total mean energy loss is $\frac{1}{2}\Delta E$ [23]. The PID value is defined as

$$\text{PID} = \Delta E_{\text{total}}\dot{E}_{\text{total}} = \Delta E(E + \frac{1}{2}\Delta E)^{c_1} \simeq AZ^2 \quad (4.9)$$

c_1 is a constant. In this analysis, c_1 was 0.75. Figure. 4.13 shows that Mass- ΔE correlation of the reaction products for Al target. The trigger condition of this figure is $BEAM \otimes SSD \otimes NEUT$ and the 5 MeV threshold of pulse height in the neutron counter was performed.

4.4.3 Improving the mass resolution of SSD

Figure 4.13 shows that the fragment was mixed with the with ^{26}Ne beam because of the energy struggling of the target . To improve the mass resolution, the position information of SSD was used(see in Fig. 4.14). The angular distribution from the position information shows that the angle of ^{26}Ne outgoing the target is forward angle because of no reaction on the target(see in Fig. 4.15). The results of the mass spectrum rejecting this component at Pb and Al targets and empty are shown in Fig.(see in Fig. 4.16, 4.17, 4.18), respectively. The table of mass resolution σ from these mass spectrum is in Table. 4.6.

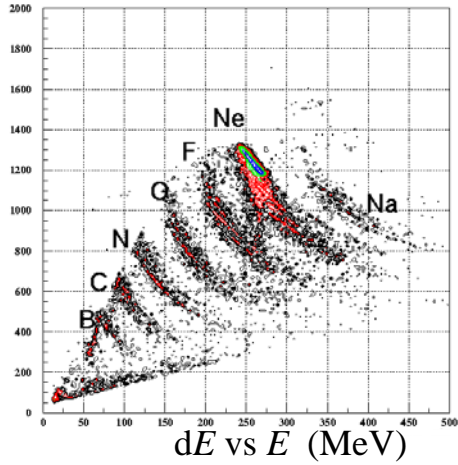


Figure 4.12: ΔE versus E of the reaction products.

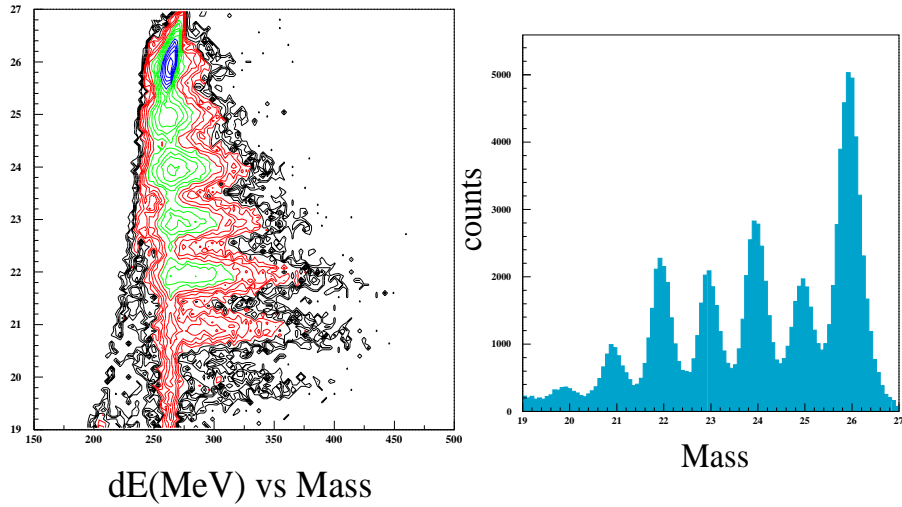


Figure 4.13: The mass versus of ΔE at Al target. The trigger condition is $BEAM \otimes SSD \otimes NEUT$. The 5 MeV threshold of pulse height on the neutron counter and multiplicity of zero on veto counters were performed. The Ne isotopes is mixed with the ^{26}Ne beam because of the energy straggling of the target.

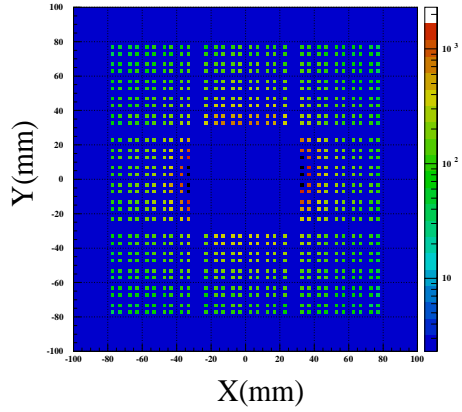


Figure 4.14: The position of SSD. The space of each strips are 5 mm.

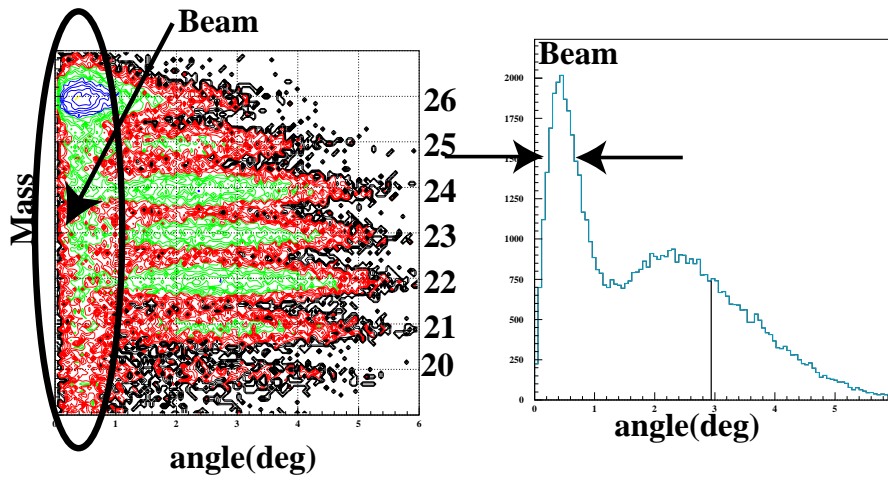


Figure 4.15: The mass versus of angular θ at Al target. The angle of ^{26}Ne beam is almost forward angle.

RUN	$^{26}\text{Ne}+\text{Pb}$	$^{26}\text{Ne}+\text{Al}$	$^{26}\text{Ne}+\text{empty}$
^{26}Ne	0.238	0.224	0.279
^{25}Ne	0.259	0.244	0.250
^{24}Ne	0.259	0.222	0.232
^{23}Ne	0.282	0.226	0.226
^{22}Ne	0.257	0.218	0.218
^{21}Ne	0.304	0.228	0.228
^{20}Ne	0.477	0.294	0.254

Table 4.6: The table of σ with Gaussian fitting of mass distribution.

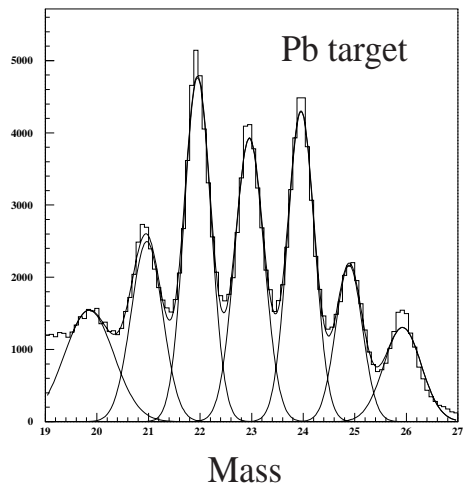


Figure 4.16: The mass identification of Ne isotopes on SSD after cutting the forward angle for Pb target.

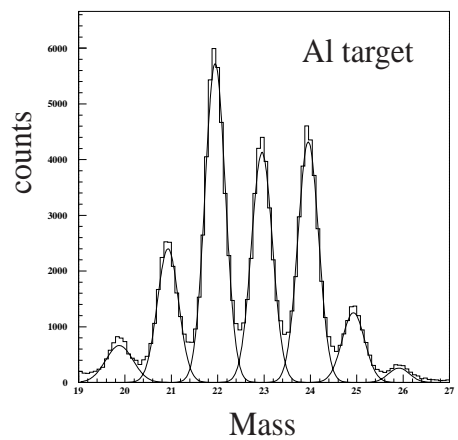


Figure 4.17: The mass identification of Ne isotopes on SSD after cutting forward angle at Al target.

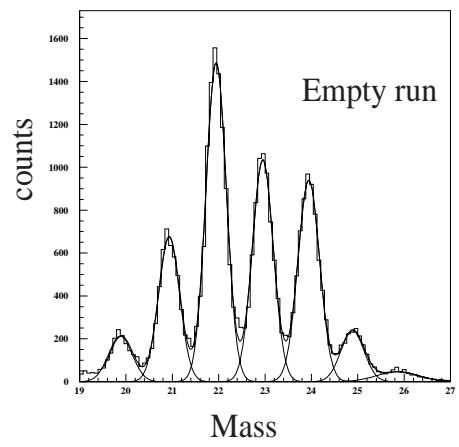


Figure 4.18: The mass identification of Ne isotopes on SSD after cutting forward angle at empty target.

4.5 Acceptance Correction of SSD

The acceptance of the SSD was estimated by a Monte Carlo simulation. We first evaluated the detector acceptance in case where the incoming beam has no angular spread. Only the detector geometry is considered in this simulation. To check this calculation, the result of the simulation was compared to the result of the analytical calculation. Analytical calculation is from the geometry information by using the Eq.4.10.

$$\epsilon = \frac{2 * \pi * r_{\text{real}}}{2 * \pi * r} \quad (4.10)$$

Figure 4.19 and Figure 4.20 show the detector acceptance as a function of angular range, where θ represents the angle of the laboratory frame. The SSD covers the angle from 1.5 degrees to 5.0 degrees.

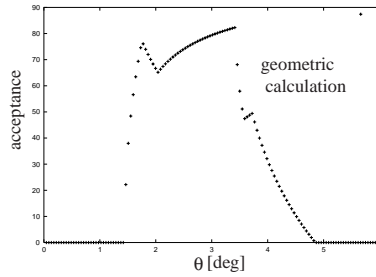


Figure 4.19: Detector acceptance of the SSD as a function of the angle in the laboratory frame. The data is obtained from the geometrical calculation.

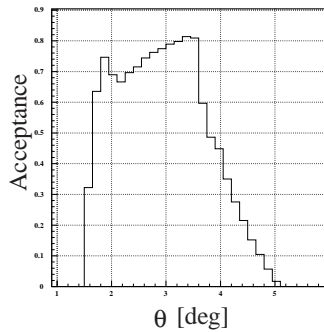


Figure 4.20: Detector acceptance of the SSD as a function of the angle in the laboratory frame. This data is obtained from the Monte Carlo simulation and Only the detector geometry is considered in the simulation.

As a next step, we took into account the finite size and the angular spread of

the incident beams. The input profile of the incident beam for the simulation is in Fig 4.21. The result of the acceptance including the beam profile is shown in Fig. 4.22. The efficiency, ratio of SSD for the fragments was estimated and the results are shown in Table. 4.7 and Fig. 4.23.

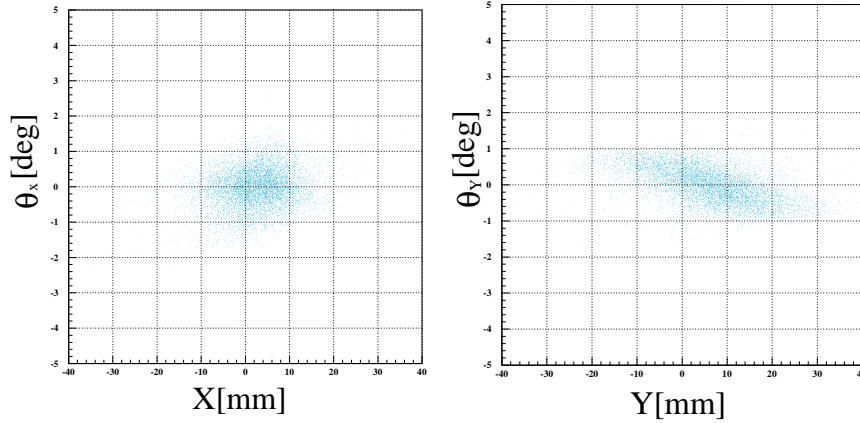


Figure 4.21: The input profiles of Y versus θ_Y , and X versus θ_X from the PPAC information. These show that the incident beam is focused on the SSD.

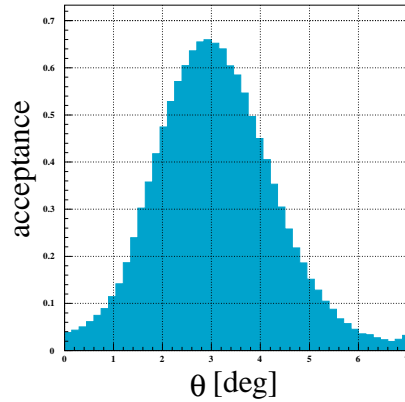


Figure 4.22: Detector acceptance of the SSD as a function of the angle in the laboratory frame from the Monte Carlo simulation. The finite size and angular spread of the incident beam is take into accounted in the data.

As a system check of the acceptance for the SSD, the cross-section obtained from $\text{Pb}(^{26}\text{Ne}, ^{26}\text{Ne}^*)$ was used. The first excited state, ($2020 \text{ KeV}:2^+ \rightarrow \text{g.s.}$) for ^{26}Ne has already been measured[21] and this cross-section has already been estimated[12]. The result of the cross section ($2020 \text{ KeV}:2^+ \rightarrow \text{g.s.}$) is shown in Fig.4.24 and Ta-

fragments(system)	before correction	after correction	ϵ
25Ne Pb(lab)	9795	46471	21.1%
25Ne Al(lab)	3445	14304	24.1%
24Ne Pb(lab)	17487	85769	20.4%
24Ne Al(lab)	9700	33806	28.7%
23Ne Pb(lab)	13994	73276	19.1%
23Ne Al(lab)	7838	23298	33.6%
22Ne Pb(lab)	15956	81470	19.6%
22Ne Al(lab)	10227	29456	34.7%

Table 4.7: The number of events between before correction of SSD and after correction.

ble.4.8.

	Pb
before	1236
after	3101
ratio	39.8
σ [mb](exp 58 MeV/nucleon)	75(15)
σ [mb](previous[12] 41.7 MeV/nucleon)	74(13)

Table 4.8: The counts of the photo-peak at 2020KeV for ^{26}Ne at Pb and Al target, respectively.

Acceptance Correction(SSD)

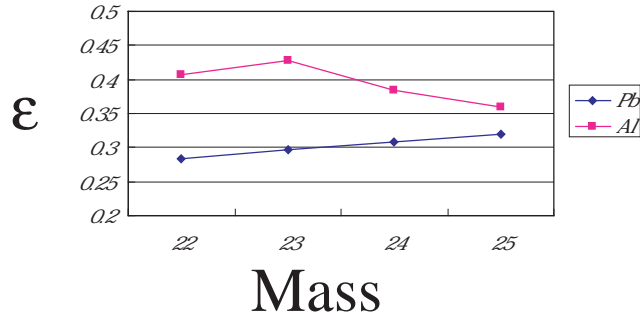


Figure 4.23: Plot of efficiency ratio for acceptance in the Ne fragment at Pb and Al, respectively.

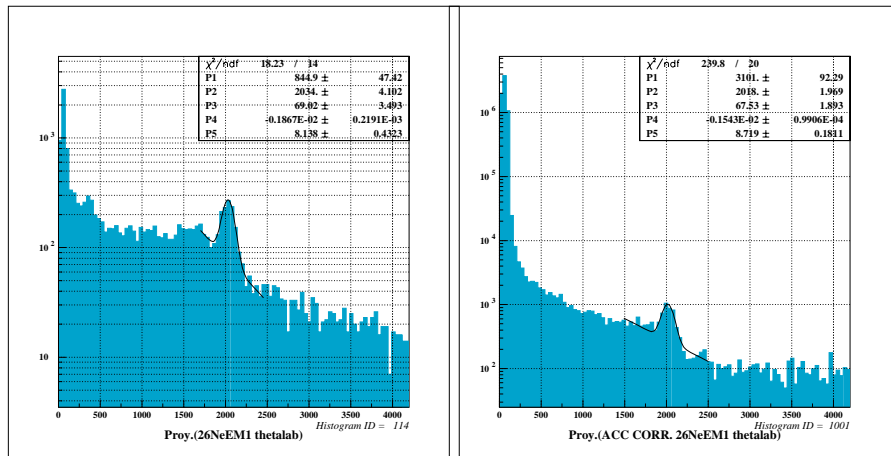


Figure 4.24: Left: The γ -ray spectrum before acceptance in the Pb target. Right: The γ -ray spectrum after the acceptance correction in SSD.

5 Result and Discussion

5.1 Reaction Cross Section

Reaction cross sections of $^{26}\text{Ne}+\text{Pb}(\text{Al})\rightarrow ^{22-25}\text{Ne}+\text{n}+\text{x}$, are listed in Table 5.1, and are also shown in Fig.5.1. Here the acceptance for the fragment in SSD is corrected, but not for the neutron. The trigger condition is $BEAM\otimes SSD\otimes NEUT$. The 5 MeV threshold of pulse height of the neutron counter, and multiplicity of zero on veto counters were set.

RUN	$^{26}\text{Ne}+\text{Pb}(\text{error})[\text{mb}]$	$^{26}\text{Ne}+\text{Al}(\text{error})[\text{mb}]$
^{25}Ne	257(6)	18(0.7)
^{24}Ne	471(5.5)	43(1.1)
^{23}Ne	403(6.1)	30(1.6)
^{22}Ne	447(6.1)	37(1.6)

Table 5.1: The list of reaction cross sections table of $^{26}\text{Ne}+\text{Pb}(\text{Al})\rightarrow ^{22-25}\text{Ne}+\text{n}+\text{x}$

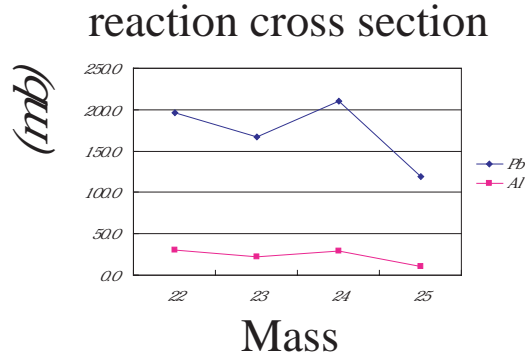


Figure 5.1: The reaction cross sections of $^{26}\text{Ne}+\text{Pb}(\text{Al})\rightarrow ^{22-25}\text{Ne}+\text{n}+\text{x}$

As a simple model to estimate the Coulomb dissociation from $^{26}\text{Ne}\rightarrow ^{22-25}\text{Ne}+\text{n}+\text{x}$ on the Pb target, the ratio, $\sigma_{\text{Pb}}/\sigma_{\text{Al}}$ was extracted. This value may be used to estimate the Coulomb dissociation contributions in the $^{26}\text{Ne}+\text{Pb}\rightarrow ^{22-25}\text{Ne}+\text{n}+\text{x}$

reaction, when we assume that the same reaction from the Al target is produced only by the nuclear breakup. From Fig. 5.2, the ratio of A=25 is larger than that of any other fragment. This contributes two probabilities on the coincidence with neutron. This enhancement for the ^{25}Ne channel may be attributed to either of the following reasons. One is the large contribution of the Coulomb dissociation for ^{25}Ne than any other channels. This makes $\sigma_{\text{Pb}}/\sigma_{\text{Al}}$ larger. The other reason may be that the different reaction mechanisms between Coulomb and nuclear breakup is seen due to the trigger condition which requires neutron detection at forward angle. In the Coulomb breakup, where momentum transfer is small, the outgoing neutron is emitted at forward angles. On the other hand for the nuclear breakup, neutron tends to be emitted at large angles except for the evaporated neutron. As will be discussed in the next section, when we assume the fragmentation process for the nuclear breakup, the cross section for ^{25}Ne nuclear breakup should be hindered. Because this channel should not have an evaporated neutron. In fact the hindrance of the cross sections for ^{25}Ne compared to ^{24}Ne is seen in Fig 5.1, in particular for Al. Since $\sigma_{\text{Pb}}/\sigma_{\text{Al}}$ is, however, largest, there should remain Coulomb breakup contribution in ^{25}Ne .

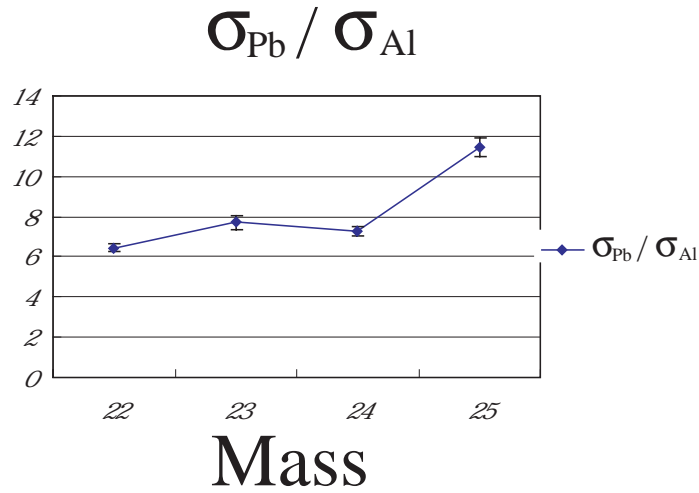


Figure 5.2: The figure of the ratio, $\sigma_{\text{Pb}}/\sigma_{\text{Al}}$. The ratio between from A=22 to A=24 are almost same ratio. This result shows this process arises from A=22 to A=24 is explained by the same reaction mechanism, nuclear reaction.

5.2 Angular distributions of Ne fragments

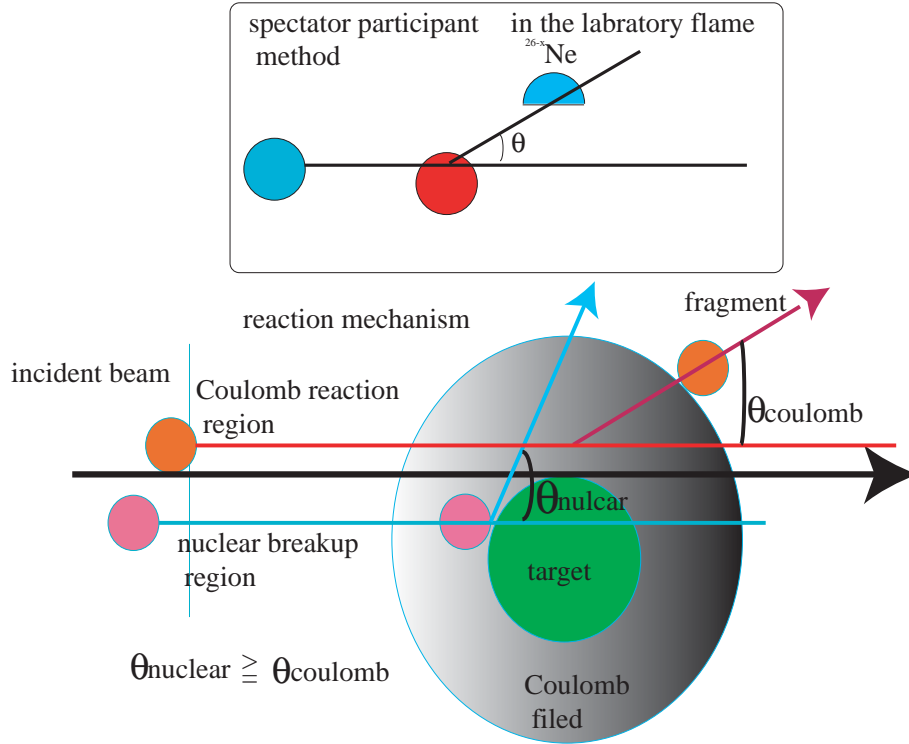


Figure 5.3: The schematic view of the Spectator Participant Method.

As discussed with previous section, the fragmentation is one of the important processes in the nuclear breakup. Here we analyze the data in terms of the fragmentation model. In this way, we attempt to develop a method to distinguish the Coulomb dissociation component from the nuclear breakup.

The fragmentation process is understood by the so called Spectator Participant model. The schematic view of the Spectator Participant model is shown in Fig.5.3. The scattering angle of the fragment by nuclear breakup is larger than that of Coulomb dissociation. Thus in the assumption that fragment is produced by both nuclear breakup and Coulomb dissociation, these reaction contribute to the angular distribution. In the nuclear breakup, Goldhaber model[3] is used to explain the momentum distribution. In the Goldhaber model, the angular distribution of the fragment in the laboratory frame is approximately described as

$$\frac{d\sigma}{d\Omega} = C_1 \exp\left(-A_F \frac{E_F \theta^2}{2\sigma_{\perp}}\right) \quad (5.1)$$

where σ_{\perp} is the variance of the momentum distribution in the perpendicular

direction.

σ_{\perp} in this model is represented as

$$\sigma_{\perp}^2 = \frac{A_F(A_P - A_F)}{A_P - 1} \sigma_0^2 + \frac{A_F(A_F - 1)}{A_P(A_P - 1)} \sigma_D^2 \quad (5.2)$$

where

- A_P : projectile mass number
- A_F : fragment mass number
- σ_0 : the width due to the Fermi momentum
- σ_D : deflection effect

The angular distributions of fragments for Al and Pb targets are shown in Fig. 5.4 and Fig. 5.5. As in this frame, angular distributions have two components, i.e, narrow and wide components. The one sigma widths σ_{\perp} for narrow and wide components were obtained by fitting the data by two Gaussian. The extracted σ_{\perp} values are shown in Fig. 5.6 and Fig.5.7 for the narrow and wide components, respectively. As shown in Fig.5.7, we have found that the wide components are almost the same irrespective of the kinds of the targets. As for the narrow components, the σ_{\perp} for Al is broader than that of Pb. We have then extracted σ_D parameter for the wide component. The obtained σ_D for Pb and Al targets are found to be almost the same result, 267(11) and 262(5), respectively for the constant value of $\sigma_0=87$ MeV/c[10](see Fig.5.7). This shows that the wide component is independent of the target, and is agreement with the Goldhaber model. For the narrow component, in the assumption of σ_0 , the deflection parameter constant σ_D was obtained to be 96(0.3) and 121(15) for Pb and Al target, respectively. One possible mechanism is that for the narrow component this component is due to the Coulomb dissociation. However the quantitative investigation for the mechanism is yet to be done.

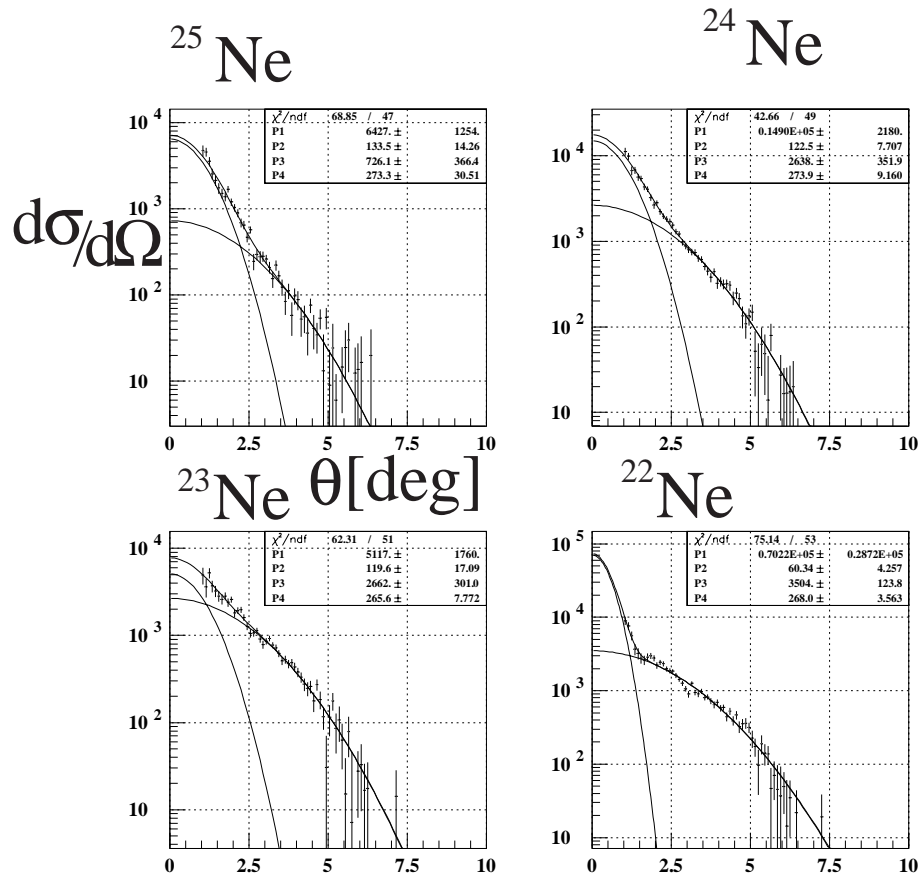


Figure 5.4: The angular distribution of fragment for Al target from A=22 to A=25 in the laboratory frame.

x

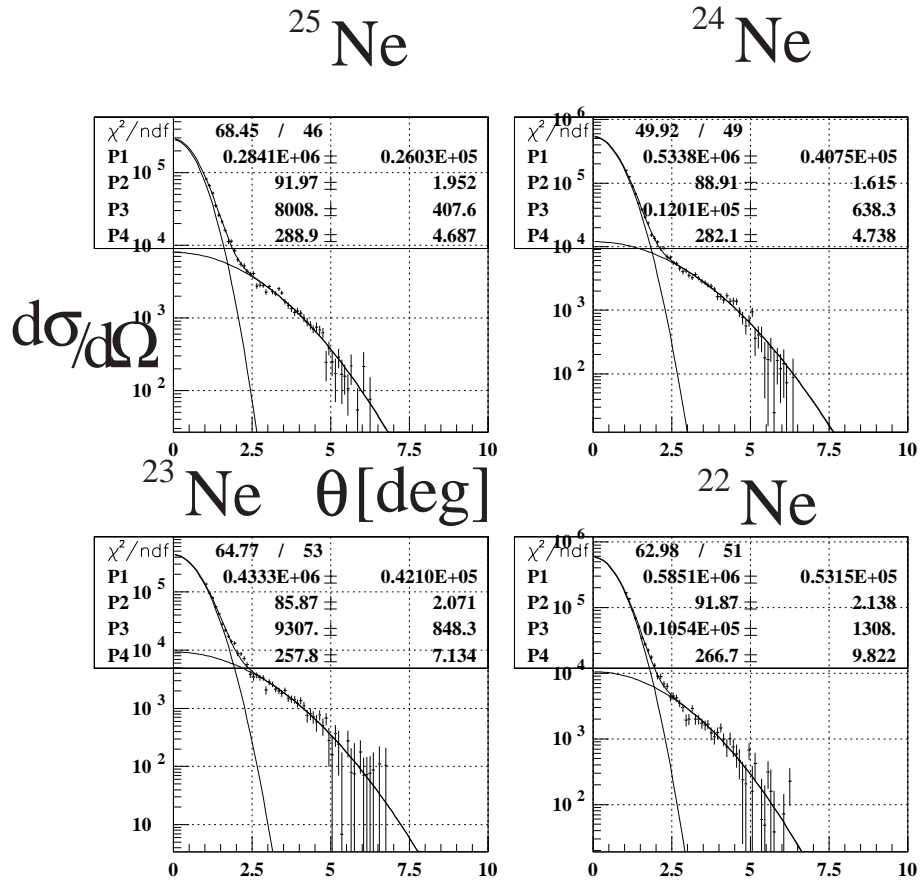


Figure 5.5: The angular distribution of fragment for Pb target from A=22 to A=25 in the laboratory frame.

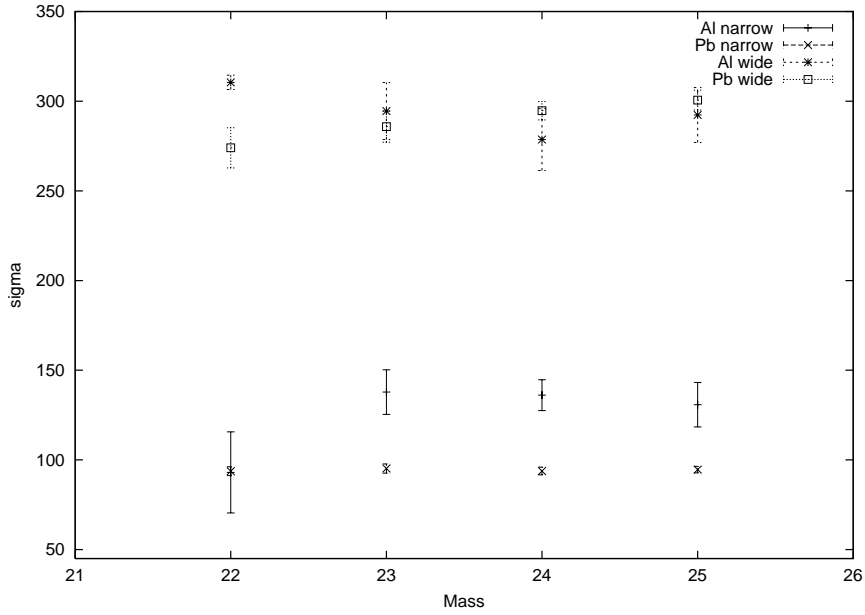


Figure 5.6: The σ_{\perp} for the narrow component and wide component respectively. The wide component is independent of the target. On the other hand, in the narrow component, the σ_{\perp} of Pb targets is smaller than the σ_{\perp} of Al target

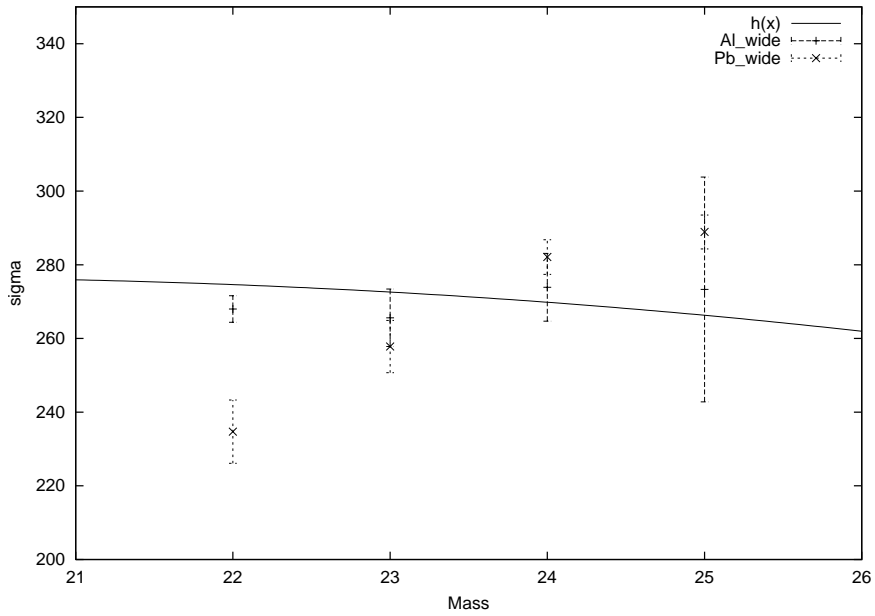


Figure 5.7: The σ_{\perp} for the wide component. The solid line is the Goldhaber model calculation. By using $\sigma_0=87$, the deflection parameter of $\sigma_d=267(11)$ and $\sigma_d = 262(4.6)$ at Pb and Al targets, and this value is independent of the target.

6 Conclusion

The study of the low-lying $E1$ strength of the neutron-rich ^{26}Ne nucleus was studied by using the Coulomb dissociation. In this thesis, the inclusive reaction cross sections and angular distributions for the breakup reaction channels $^{26}\text{Ne}+\text{Pb}\rightarrow^{22-25}\text{Ne}+\text{n}+\text{x}$, $^{26}\text{Ne}+\text{Al}\rightarrow^{22-25}\text{Ne}+\text{n}+\text{x}$ were analyzed to develop a method to distinguish the Coulomb dissociation component from the nuclear breakup.

By the analysis of reaction cross section, we obtain the possibility of Coulomb breakup contribution in ^{25}Ne . This result was derived to the ratio, σ_{Pb}/σ_{Al} from $^{26}\text{Ne}+\text{Pb}(\text{Al})\rightarrow^{22-25}\text{Ne}+\text{n}+\text{x}$. In the assumption that the same reaction from the Al target is produced only by the nuclear breakup, this value may be used to estimate the Coulomb dissociation contributions. The ratio of A=25 is larger than that of any other fragment.

In the angular distributions for the breakup reaction, angular distributions have two component, i.e, narrow and wide components. For the wide component, the angular distribution is independent of the target. Therefore, this result is agreement with Goldhaber model. But for the narrow component, the quantitative investigation for the mechanism is yet to be done. In the next step, we should reconstruct the relative energy spectrum $^{25}\text{Ne}+\text{n}$.

A Appenidx

A.1 Coulomb Potential

Coulomb potential is

$$U(r) = \frac{Z_1 Z_2 e^2}{4\pi\epsilon r} = \frac{\alpha\hbar c}{r} Z_1 Z_2 \quad (\text{A.1})$$

where

- $U(r)$: Coulomb potential
- r : Sum of the target and the projectile radius
- Z_1, Z_2 : atomic number
- e : charge of electron
- α : coupling constant $\simeq 1/137$
- $\hbar c \simeq 200 \text{ MeVfm}$

In the experiment, the incident beam and the reaction target are ^{26}Ne and ^{208}Pb , respectively. Therefore, Z_1 and Z_2 are 10 and 82, respectively. Radius of the projectile and the reaction target are 2.86 fm [22] and 7.1 fm from the standard estimation $1.2 \times A^{1/3}$, respectively.

$$U = \frac{\alpha\hbar c}{R_1 + R_2} Z_1 Z_2 = \frac{1}{137} \times 200 \times \frac{1}{7.1 + 2.86} \times 10 \times 82 [\text{MeV}] \simeq 120 \text{ MeV} \quad (\text{A.2})$$

In the kinetic energy of the incident beam,

$$E_{\text{rel}} = E_{\text{in}} \frac{M_{\text{tgt}}}{M_{\text{tgt}} + M_{\text{beam}}} \quad (\text{A.3})$$

where

- E_{rel} : relative energy between the target and incident beam
- E_{in} : kinetic energy of the incident beam
- $M_{\text{beam}}, M_{\text{tgt}}$: mass of the incident and target, respectively

In this experiment, the energy of the incident beam is 58 MeV/u. The relative energy is the following.

$$E_{\text{rel}} \simeq 1400 \text{ MeV (Pb)}$$

Therefore,

$$E_{\text{rel}} \gg U(r)$$

A.2 Analysis PPAC

The following picture is the schematic view of the PPAC definition.

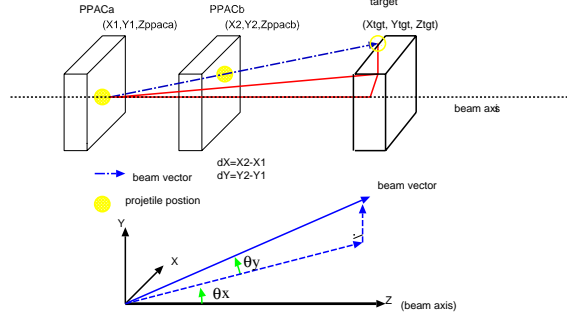


Figure A.1: PPAC definition θ_x (2) θ_y

Position of X and Y was calculated from both side signals on the X and Y strip, respectively.

$$T_{\text{left}} - T_{\text{right}} = \frac{X}{V} - \frac{L - X}{V} \propto X \quad (\text{A.4})$$

where

- V: velocity of the current at strip
- L: length
- X: position of the incident beam

The definition of X, Y and Z is shown in the Fig A.1. The incident angle θ , θ_x and θ_y of the beam is calculated by using the position information of the PPAC-A and PPAC-B in Eq[?, ?].

$$\theta_x = \tan^{-1} \frac{dX}{Z_{\text{PPACB}} - Z_{\text{PPACA}}} \quad (\text{A.5})$$

$$\theta_y = \tan^{-1} \frac{dY}{Z_{\text{PPACB}} - Z_{\text{PPACA}}} \quad (\text{A.6})$$

- dX: $X_{\text{PPACB}} - X_{\text{PPACA}}$
- dY: $Y_{\text{PPACB}} - Y_{\text{PPACA}}$

From θ_X, θ_Y , the image of the incident beam at target was extrapolated.

$$X_{\text{target}} = X_{\text{PPACA}} + dX \frac{Z_{\text{target}} - Z_{\text{PPACA}}}{Z_{\text{PPACB}} - Z_{\text{PPACA}}} \quad (\text{A.7})$$

$$Y_{\text{target}} = Y_{\text{PPACA}} + dY \frac{Z_{\text{target}} - Z_{\text{PPACA}}}{Z_{\text{PPACB}} - Z_{\text{PPACA}}} \quad (\text{A.8})$$

The momentum vector of the incident beam was measured by using the momentum from TOF at F2PL, and the incident angle of PPAC.

$$P_X = P_{\text{beam}} \frac{\tan \theta_X}{\sqrt{1 + \tan^2 \theta_X + \tan^2 \theta_Y}} \quad (\text{A.9})$$

$$P_Y = P_{\text{beam}} \frac{\tan \theta_Y}{\sqrt{1 + \tan^2 \theta_X + \tan^2 \theta_Y}} \quad (\text{A.10})$$

$$P_Z = \sqrt{P_{\text{beam}}^2 - P_X^2 - P_Y^2} \quad (\text{A.11})$$

- P_{beam} : beam momentum measured by F2PL
- P_X, P_Y, P_Z : X, Y and Z components of the beam momentum, respectively

A.3 Analysis of Gamma Rays

A.3.1 Energy calibration

The analog data of DALI taken by the ADC modules were calibrated by using standard γ -ray sources of ^{22}Na (511 keV and 1275 keV), ^{60}Co (1173 keV and 1333 keV), ^{137}Cs (662 keV), and the mixture of Am-Be (4439 keV, 3928 keV and 3417 keV). The process of γ -rays from the mixture of Am-Be source is explained in the appendix. Table. A.3.1 shows the resolute of the DALI calibration.

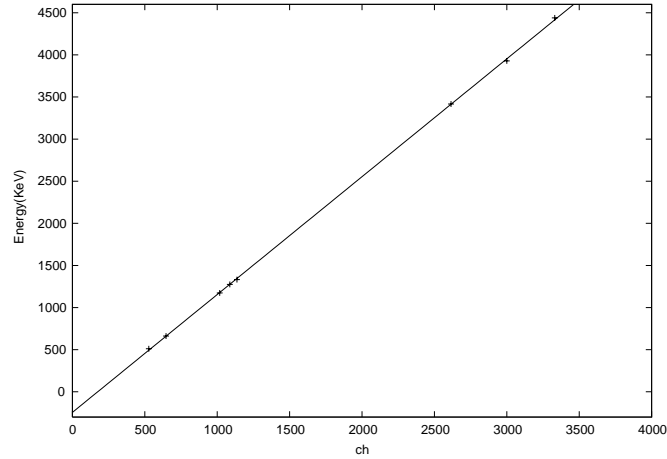


Figure A.2: ch versus keV

source	Energy(KeV)	exp Energy(KeV)	deviation(KeV)
^{137}Cs	661.660	660.7	-0.3
^{60}Co	1173.237	1174.	0.6
	1332.501	1335.	2.5
^{22}Na	1274.532	1276.	1.5
	511	506.2	-4.8
$^9\text{Be}+^{241}\text{Am}$	4439.1	4428.	-11.1
	3928.1	3955.	27.
	3417.1	3402.	-15.

The function is

$$E_{\gamma} = c_1 E_{\text{ch}} + c_2 \quad (\text{A.12})$$

A.3.2 Timing Gate for Background Reduction

The γ -ray detectors were sensitive not only to the γ rays from the reaction products but also to the charged particle, neutrons, γ rays from the detectors, and natural background γ rays. In order to select true coincidence events, a gate width of γ -ray detection time was set. Figure A.3 shows a time spectrum of the NaI(Tl) scintillation detectors. The timing data were calibrated in the same way as described in Beam line section.

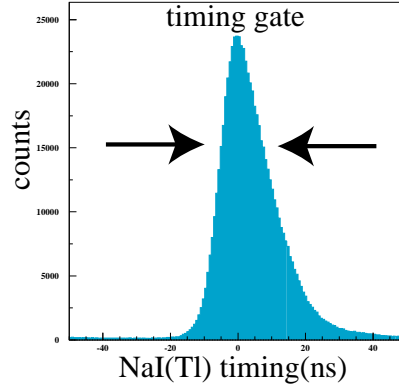


Figure A.3: Time spectrum of NaI(Tl) scintillators detectors. The γ -rays from the reaction products are selected by the gates indicated by the Gaussian component. The constant component was due to the background components.

Fitting function is

$$Y = c_1 \exp\left[-\frac{(T - c_2)^2}{2c_3^2}\right] + c_4 \quad (\text{A.13})$$

- $T = T_{\text{F2PL}} - T_{\text{DALI}}$

The constant c_4 is independent of timing. This is interpreted as background components. To select Gaussian component in Fig. A.3, a clear peak corresponding to the true coincidence events can be taken.

A.4 Doppler shift correction

In this experiment, we detected γ -rays emitted from moving reaction products with a velocity $v/c \sim 0.32$. Hence Doppler-shifted γ -ray energies were measured by the γ -ray detectors.

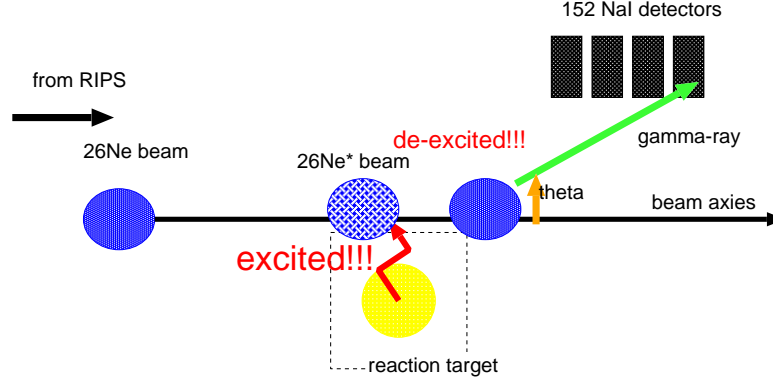


Figure A.4: Schematic view of in-beam γ spectroscopy. The theta is the γ -ray detection angle with respect to the beam axis in the laboratory frame.

The γ -ray energy in the rest frame of the incident particle E_{γ}^{proj} and the γ -ray energy in the laboratory frame E_{γ}^{lab} are connected by the velocity of the incident particle and the γ -ray detection angle with respect to the beam axis in the laboratory frame θ . The introduction of the Doppler shift corrected spectrum is given by the following.

$$\begin{pmatrix} E_{\gamma}^{\text{proj}}/c \\ P^{\text{proj}} \end{pmatrix} = \begin{pmatrix} \gamma & -\beta\gamma \\ -\beta\gamma & \gamma \end{pmatrix} \begin{pmatrix} E_{\gamma}^{\text{lab}}/c \\ P^{\text{lab}} \end{pmatrix}$$

- E_{γ}^{proj} : γ energy in the rest frame of the incident particle
- P^{proj} : γ particle momentum in the rest frame of the incident particle
- E_{γ}^{lab} : γ energy in the laboratory frame
- P^{lab} : γ particle momentum in the laboratory
- β : relativistic velocity
- γ : Lorentz factor $1/\sqrt{1-\beta^2}$

$$E_{\gamma}^{\text{proj}}/c = \gamma E_{\gamma}^{\text{lab}}/c - \gamma\beta P^{\text{lab}} \quad (\text{A.14})$$

Relativistic velocity is the

$$\beta = \hat{\beta} \cos \theta \quad (\text{A.15})$$

- $\hat{\beta}$: β of the production products
- θ : laboratory angle with respect to the beam axis

$$E_{\gamma}^{\text{lab}} = h\nu \quad (\text{A.16})$$

$$P = \frac{h}{\lambda} = \frac{h\nu}{c} \quad (\text{A.17})$$

$$\frac{P}{E_{\gamma}^{\text{lab}}} = \frac{1}{c} \quad (\text{A.18})$$

Therefore,

$$E_{\gamma}^{\text{proj}} = E_{\gamma}^{\text{lab}} \gamma (1 - \beta \cos \theta) \quad (\text{A.19})$$

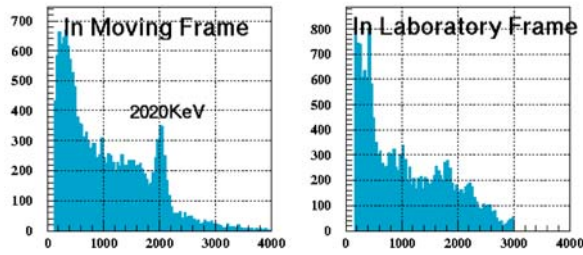


Figure A.5: Energy spectrum of γ rays detected in coincidence with the ^{26}Ne reaction products. (right) Energy spectrum in laboratory frame. (left) Doppler-corrected γ rays energy spectrum with $\beta=0.32$. The peaks at 2020 keV is clearly seen while they are vague in right indicating good quality of the Doppler correction.

A.4.1 Result of the obtained spectrum from Ne isotopes

fragment	E(exp)[keV]	σ	E(previous)[keV]	deviation[keV]	state
²⁶ Ne	2020	109	2020	0	(2 ⁺ → <i>g.s.</i>)
²⁵ Ne	1688	89	1702	-14	unknown
²⁴ Ne	1978	98	1981.6	3.6	2 ⁺ → <i>g.s.</i>
²³ Ne	1716	134	1701	15	7/2 → <i>g.s.</i>
	1294	170	1298	-4	5/2 ⁺ → 1/2 ⁺
	1001	159	1017	-16	1/2 ⁺ → <i>g.s.</i>
	785	120	805	-20	3/2 ⁺ → 1/2 ⁺
²² Ne	1263	85	1274.5	-11	2 ⁺ → <i>g.s.</i>
	848	171	-	-	-

Table A.1: Gamma-ray energies of Ne isotopes from A of 26 to A of 22. The energies deduced in the present work are compared with the literature values.

A.4.2 Energy resolution of the Doppler corrected γ -ray spectrum

Due to the finite accuracy of angular information and the velocity spread of the projectiles, the γ -ray energy peaks were broadened compared to the intrinsic energy resolution of the detectors. Based on equation A.19, the resolution E_{γ}^{proj} is approximated,

$$\left(\frac{\Delta E_{\gamma}^{proj}}{E_{\gamma}^{proj}}\right)^2 = \left(\frac{\beta \sin \theta_{\gamma}^{lab}}{1 - \beta \cos \theta_{\gamma}^{lab}}\right)^2 (\Delta \theta_{\gamma}^{lab})^2 + \left(\frac{\beta \gamma^2 (\beta - \cos \theta_{\gamma}^{lab})}{1 - \beta \cos \theta_{\gamma}^{lab}}\right)^2 \left(\frac{\Delta \beta}{\beta}\right)^2 + \left(\frac{\Delta E_{\gamma}^{lab}}{E_{\gamma}^{lab}}\right)^2 \quad (\text{A.20})$$

source	¹³⁷ Cs	⁶⁰ C		²² Na		Am-Be		
Energy[keV]	661	1173	1332	511	1274	3417	3928	4428
σ [keV]	26	32	36	25	36	84	105	95

Table A.2: The energy resolution of the obtained value from the standard γ source.

From the correlation between energy and σ , the intrinsic energy resolution of the detectors is introduced as following.

$$\sigma = 1.9\sqrt{E} - 26.97 \quad (\text{A.21})$$

Energy resolutions are evaluated using realistic condition, β of 0.32 and γ of 1.06 with $\Delta\theta_{\text{max}}$ of 20 degrees in laboratory frame of 90 degrees and $\Delta\theta_{\text{min}}$ of 0 degrees in laboratory frame of 0 degrees respectively, $\Delta\beta/\beta$ of 11.5% including the energy loss in the secondary target. $\Delta E_{\gamma}^{\text{lab}}$ is the σ from A.4.2.

fragment	²⁶ Ne	²⁵ Ne	²⁴ Ne	²² Ne
Energy[keV]	2020	1688	1978	1263
σ [exp][keV]	109	89	98	85
σ [calc][keV]	121	102	119	78

Table A.3: Energy resolution σ of the obtained Doppler corrected spectrum. The σ in the present work compared to the calculated σ .

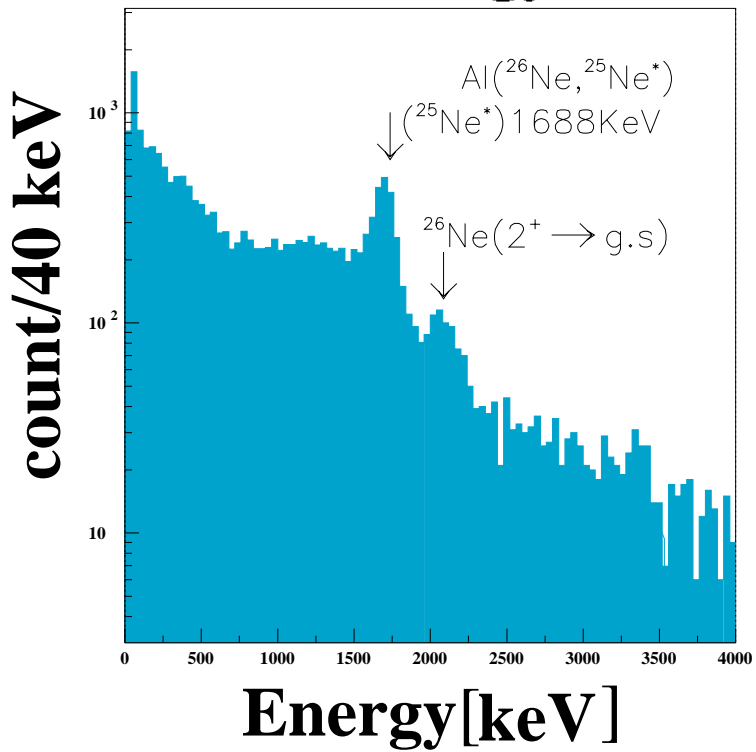
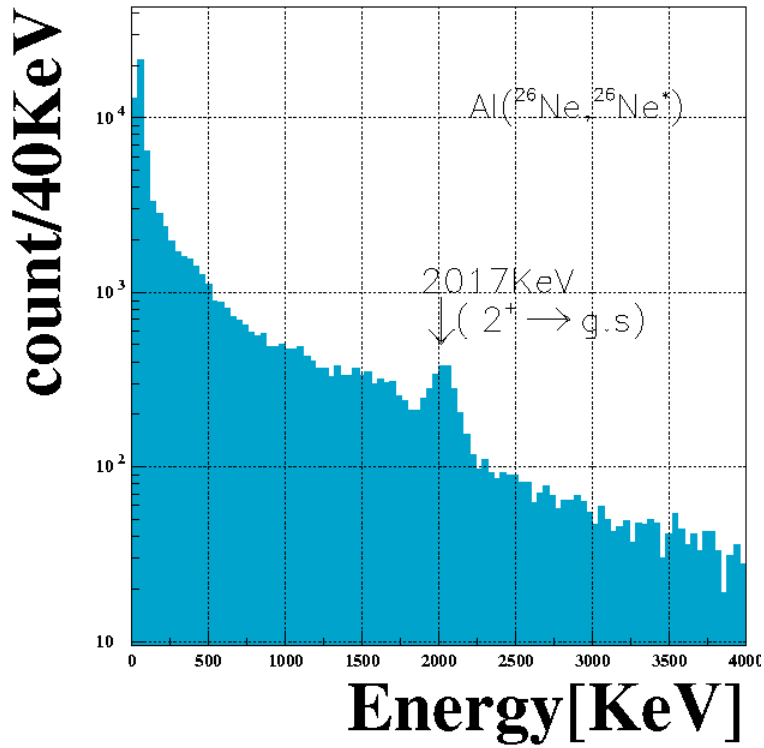


Figure A.6: Gamma-ray energy spectra obtained in coincidence with the reaction products $^{26}\text{Ne}, ^{25}\text{Ne}$.

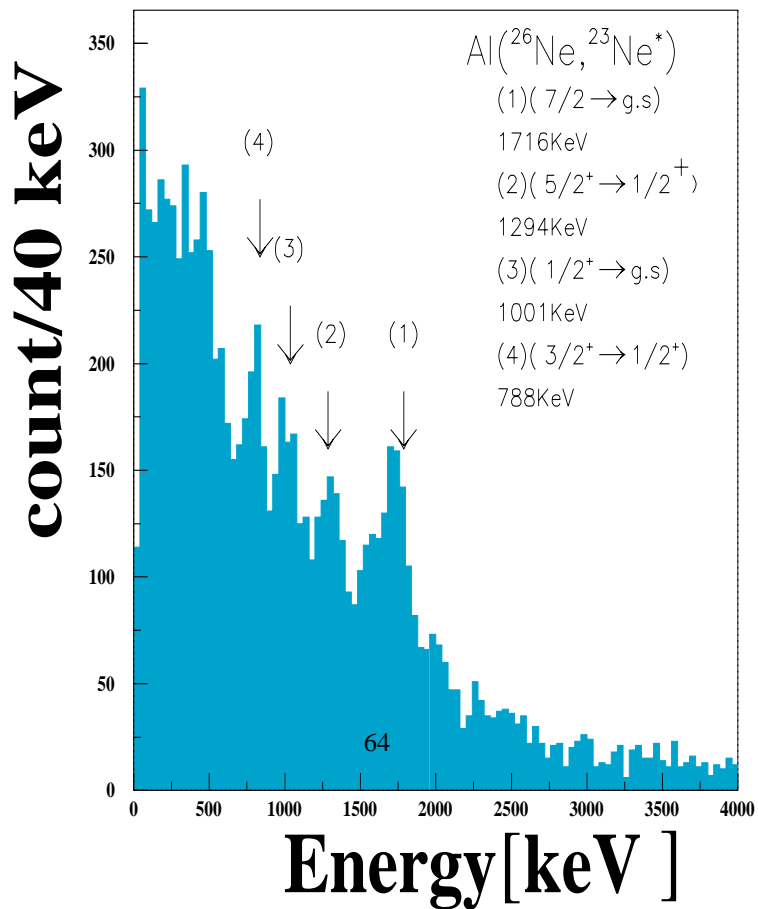
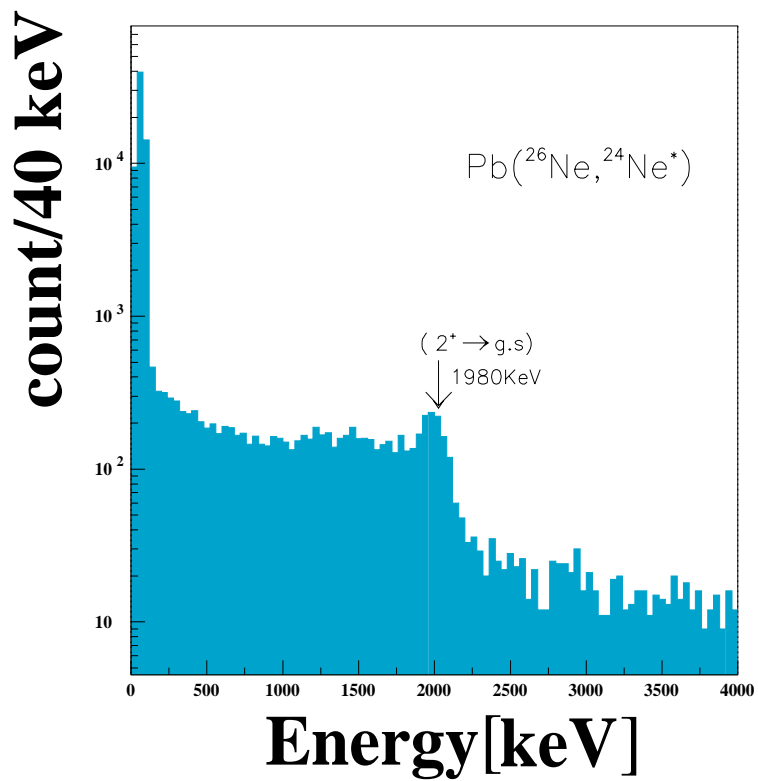


Figure A.7: Gamma-ray energy spectra obtained in coincidence with the reaction

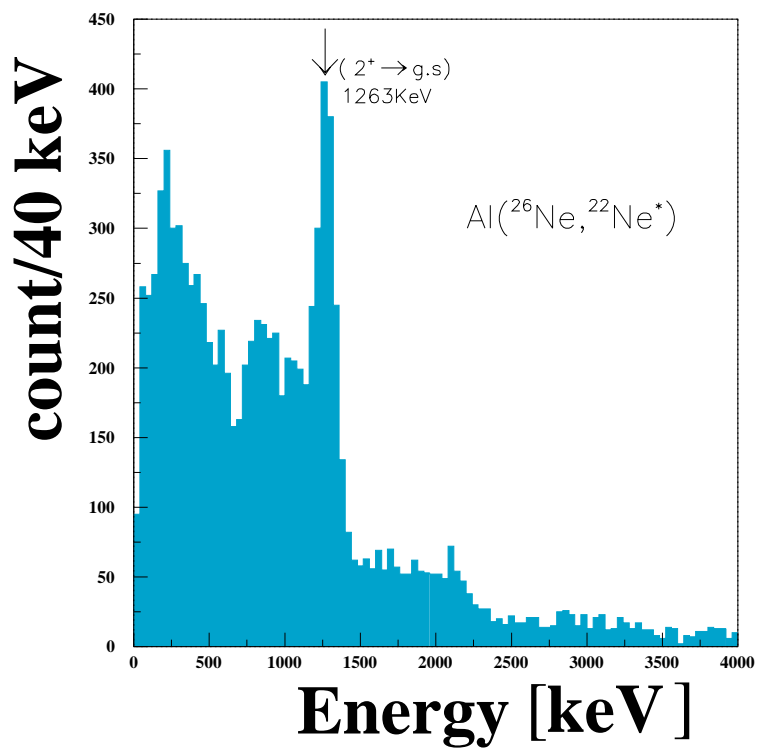


Figure A.8: Ne fragments gamma ray spectrum

Figure A.9: Gamma-ray energy spectra obtained in coincidence with the reaction products ²²Ne.

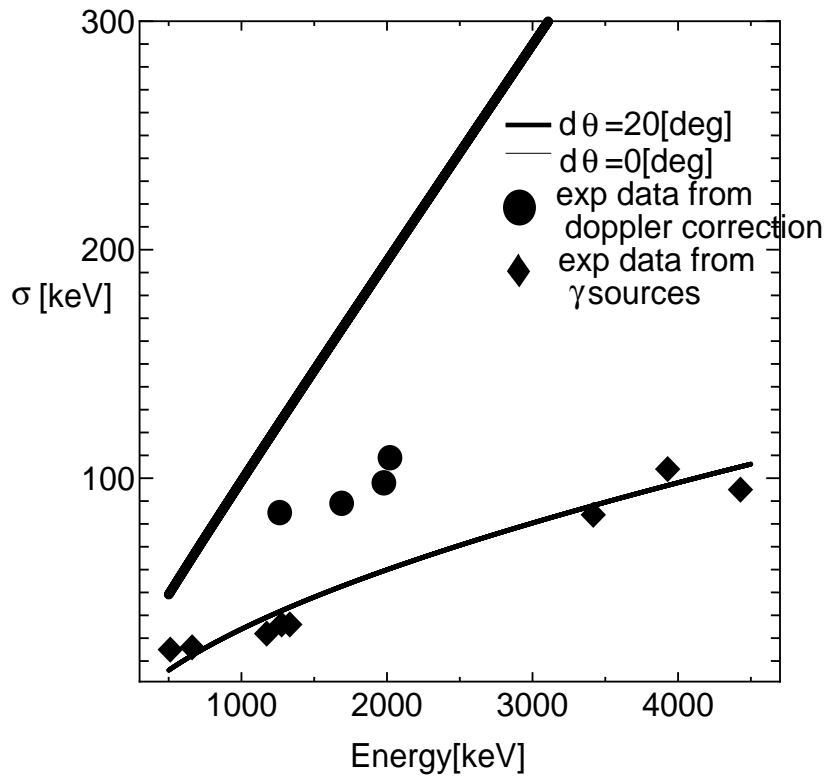


Figure A.10: Energy resolution function of γ -ray energy emitted from moving sources .

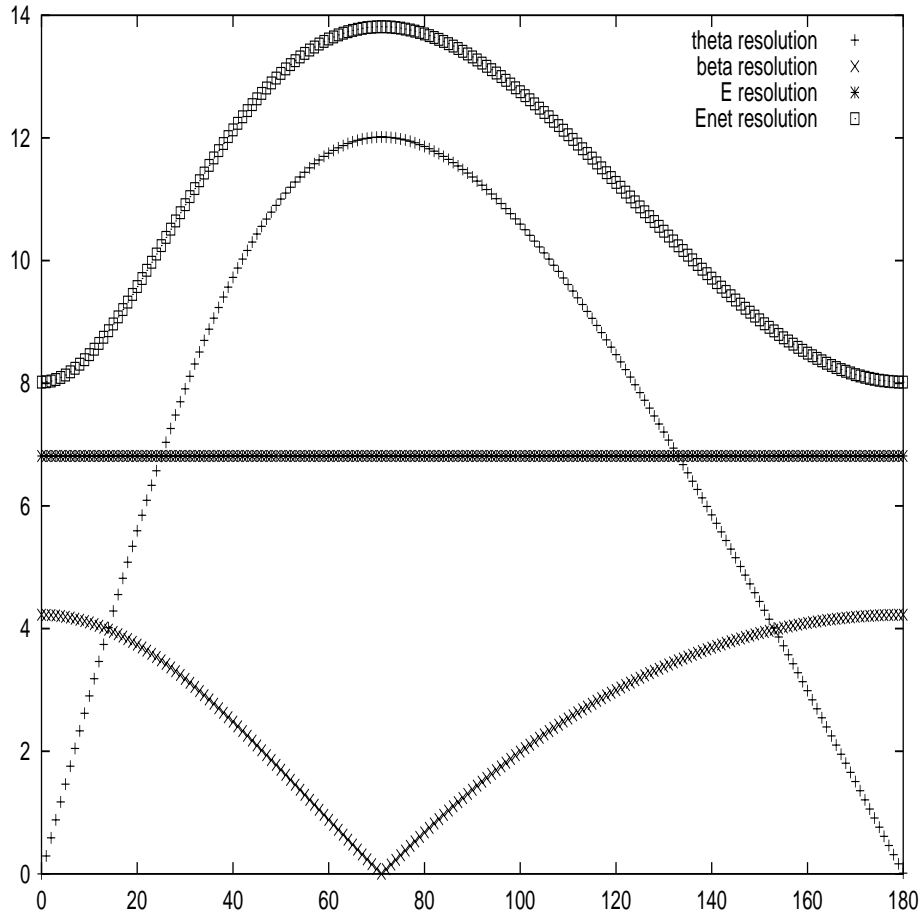


Figure A.11: Energy resolutions for 2 MeV γ -ray emitted from moving sources with $v/c \approx 0.32$. E_{net} is the energy resolution of the Doppler corrected spectrum.

B Appendix on NaI

B.1 Decay Table

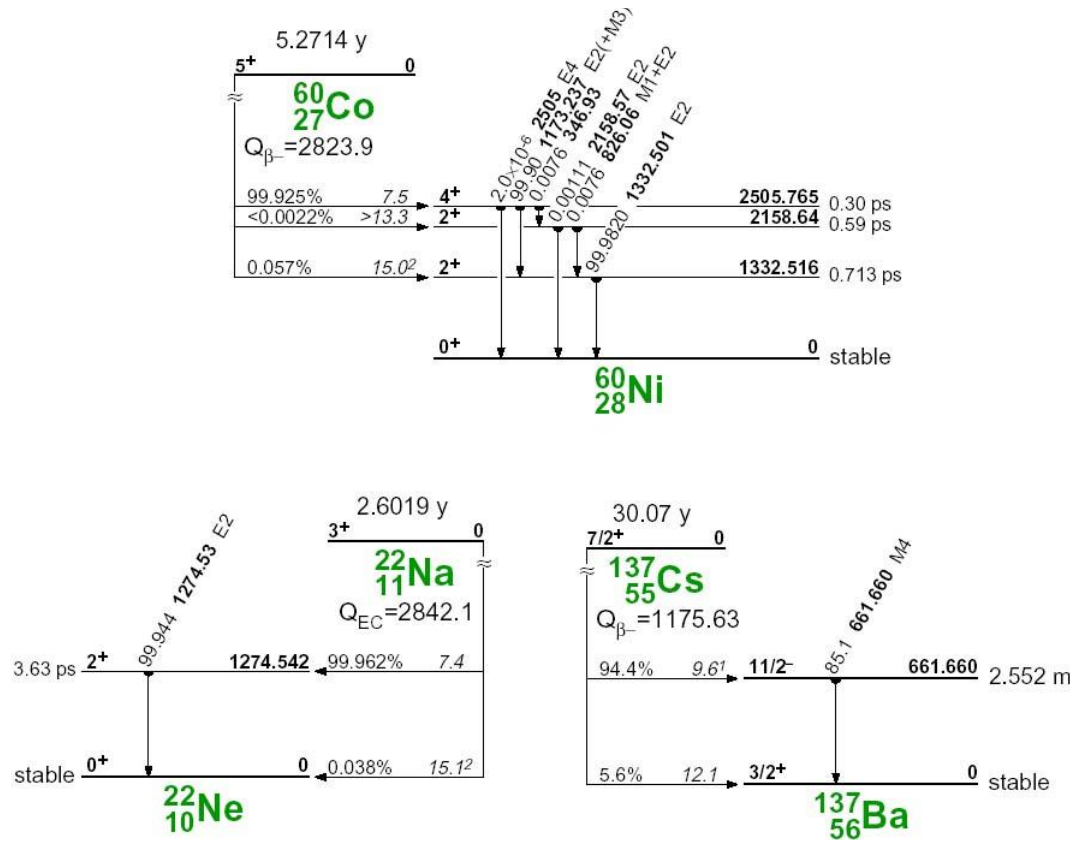
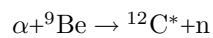
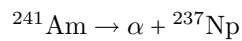


Figure B.1: Decay table used by in this experiment.

The standard γ -ray sources of ^{137}Cs , ^{22}Na , ^{60}Co and the mixture of ^{241}Am - ^9Be were used in this experiment.

In the mixture of ^{241}Am and ^9Be ,



$^{12}\text{C}^*$ is immediately de-excited to the ground state by emitting γ -ray at 4.391 MeV. High energy γ -rays produce pair productions more than the low energy γ -ray.

$$\gamma \rightarrow e^- + e^+$$

$e^+ e^-$ annihilation produced in the matter and then, two γ -ray, 511 keV were produced. In case of the NaI scintillation detectors depositing the energy contained two γ -ray, the total energy deposited in the NaI scintillation detector is same as γ -ray energy from de-excited states. In the ^{12}C , this energy is corresponding to the 4.391 MeV. In case of one γ -ray of two γ -ray escaping from the detector, NaI scintillation detectors deposits the energy corresponding to the

$$E_{\text{detected}} = E_{\gamma} - m_e c^2$$

In the ^{12}C , this energy is corresponding to the 3.928 MeV. In case of two γ -ray escaping from that, NaI deposits the energy corresponding to the

$$E_{\text{detected}} = E_{\gamma} - 2m_e c^2$$

In the ^{12}C , this energy is corresponding to the 3.417 MeV.

In $^{12}\text{C}^*$, three type spectrum of energy, 4.439 MeV, 3.928 MeV and 3.417 MeV were detected in the NaI scintillation detectors.

B.1.1 Decay formula

$$\begin{aligned} A &= -\tau \frac{dN}{dt} = \tau N \\ N(t) &= N(0)e^{-t/\tau} \\ \tau &= t_{1/2} \log 2 \end{aligned}$$

- A: number of decay
- τ : decay constant
- $t_{1/2}$: half time
- $N(t)$: yield

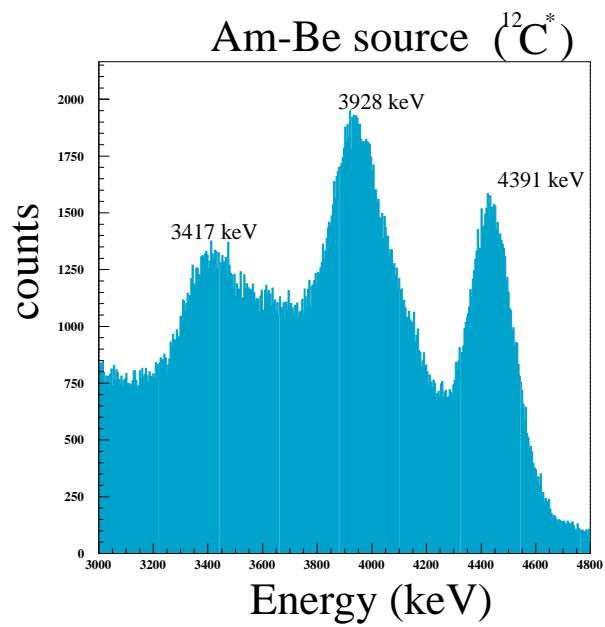


Figure B.2: γ -ray from the mixture of Am-Be sources. Be absorbed α from *alpha* decay of Am and then $^{12}\text{C}^*$ was produced. From the γ rays from $^{12}\text{C}^*$, the three type spectrum of energy, 4.439 MeV, 3.928 MeV and 3.417 MeV were detected in the NaI scintillation detectors

B.2 Efficiency calculation of the DALI

The efficiency of the DALI for the 2 MeV γ ray was estimated by **GEANT** code[?]. The energy of 2 MeV γ ray was for the To check the efficiency, γ -ray detection efficiencies were checked by using standard γ -ray sources. The standard sources, ^{137}Cs , ^{22}Na and ^{60}Co were used.

$$\epsilon = \frac{Yield_{\text{detected}}}{Yield_{\text{emission}}} \quad (\text{B.1})$$

source	^{137}Cs	^{22}Na	^{60}Co
Energy[keV]	661	1173,1332	511,1274
intensity(T=0)[kBq]	46.6	359	41.2
half time($t_{1/2}$)[year]	30.07	2.6019	5.2714
emission probability[%]	0.8521	0.999,0.9998	0.9994

Table B.1: Table of standard γ source data used in this experiment.

The efficiency from the standard γ sources was estimated as follows.

source	^{137}Cs	^{60}C	^{22}Na		
Energy[keV](exp)	661	1173	1332	511	1274
$Yield_{\text{emission}}$	4.25×10^7	3.82×10^7	3.82×10^7	2.20×10^8	1.10×10^8
$Yield_{\text{detected}}$	3.17×10^4	1.96×10^5	1.77×10^5	6.40×10^5	1.74×10^5
$Yield_{\text{detected}}$ (calibrated)	1.35×10^6	6.31×10^6	5.70×10^6	7.80×10^7	2.14×10^7
efficiency[%]	31.7	16.5	14.9	35.4	19.4

Table B.2: Table of efficiency for standard γ -ray sources.

$Yield_{\text{detected}}$ (calibrated) means

$$Yield_{\text{detected}}(\text{calibrated}) = \frac{N_{\text{ungatedevent}}}{N_{\text{gatedevent}}} * (\text{DS} - \text{DALI trigger}) * Yield_{\text{detected}} \quad (\text{B.2})$$

- DS-DALI trigger: Down scale factor
- $\frac{N_{\text{ungatedevent}}}{N_{\text{gatedevent}}}$: livetime of DALI trigger
- $Yield_{511} = 2 * Yield_{1274\text{KeV}}$ in ^{22}Na

Energy[keV]	661	1173	1332	511	1274	$E(2020\text{keV}; 2^+ \rightarrow \text{g.s})$
efficiency[%](cal)	31.0	20.2	18.5	38.4	19.1	13.6

Table B.3: The efficiency calculated from **GEANT**.

The efficiency for the 2 MeV γ ray by using **GEANT** code which reproduces well the measured efficiencies was estimated.

Figure B.2 shows plot of the photo-peak efficiencies as a function of γ -ray energies. The solid line was calculated by **GEANT** code. For 2 MeV, efficiencies was estimated attained to be about 13.6 % and this curve is within the 20% deviation. In 2 MeV γ -ray, the efficiency was 13.9 % and the systematic error, $\Delta\epsilon$ from this figure was 20%, respectively.

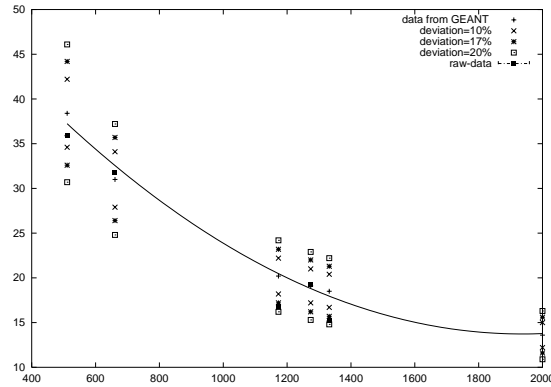


Figure B.3: Plot of photo-peak efficiencies as a function of γ -ray energies. The values measured by using γ -rays standard sources are plotted. The solid line represents the calculated values by **GEANT** code, which reproduces well measured efficiencies.

C Cross Section Estimation

C.1 formula

Cross section σ is given by

$$\sigma = \frac{N_{\text{fragment}}}{N_{\text{beam}}} \frac{A}{tN_A} \epsilon \quad (\text{C.1})$$

- σ_{reaction} : cross section
- N_{reaction} : number of reaction events
- N_B : number of the incident ^{26}Ne beam
- $A[\text{g/mol}]$: mass number
- $t[\text{g}/\text{cm}^2]$: thickness of the target
- $N_A[1/\text{mol}]$: Avogadro's number
- ϵ : correction term

The correction term, ϵ includes the efficiency and the acceptance of the detectors.

In this experiment,

- $A=208[\text{Pb}]$
- $t=0.230[\text{g}/\text{cm}^2]$

$$\frac{A}{tN_A} = 149.64 * 10^{-27} m^2 \quad (\text{C.2})$$

- $A=27[\text{Al}]$
- $t=0.130[\text{g}/\text{cm}^2]$

$$\frac{A}{tN_A} = 34.48 * 10^{-27} m^2 \quad (\text{C.3})$$

The incident N_{beam} can be estimated by using *DSBEAM* trigger which monitors the beam profile during the experiment.

$$N_{\text{beam}} = (\text{DS} - \text{factor}) * N_{26\text{Ne}} * (\text{LiveTime})_{\text{DSBEAM}} \quad (\text{C.4})$$

- ϵ : correction of the detectors
- DS-factor: 500 of the down scale factor
- $(\text{LiveTime})_{\text{DSBEAM}}$: live time for *DSBEAM* trigger

DS-factor and Live time, respectively, are

$$(\text{DS} - \text{factor}) = \frac{N_{\text{beam}}(\text{scaler})}{N_{\text{DS}}(\text{scaler})} \quad (\text{C.5})$$

$$(\text{LiveTime})_{\text{DS}} = \frac{(\text{DS} - \text{beam}_{(\text{raw}-\text{data})})}{(\text{DS} - \text{beam}_{(\text{scaler})})} \quad (\text{C.6})$$

The reaction products of N_{fragment} at *BEAM* \otimes *SSD* \otimes *NEUT* and *BEAM* \otimes *SSD* \otimes *DALI*, respectively, are as follows.

In case of *BEAM* \otimes *SSD* \otimes *NEUT* trigger,

$$N_{\text{fragment}} = N_{\text{raw-data}} * (\text{Livetime})_{\text{b}\otimes\text{s}\otimes\text{n}} * \epsilon_{\text{ssd}} \quad (\text{C.7})$$

$$(\text{LiveTime})_{\text{b}\otimes\text{s}\otimes\text{n}} = \frac{N_{\text{b}\otimes\text{s}\otimes\text{n}}(\text{raw} - \text{data})}{N_{\text{b}\otimes\text{s}\otimes\text{n}}(\text{scaler})} \quad (\text{C.8})$$

- $(\text{Livetime})_{\text{b}\otimes\text{s}\otimes\text{n}}$: live time for *BEAM* \otimes *SSD* \otimes *NEUT* trigger
- ϵ_{ssd} : acceptance correction of SSD

In the case of *BEAM* \otimes *SSD* \otimes *DALI* trigger,

$$N_{\text{fragment}} = N_{\gamma} * (\text{Livetime})_{\text{b}\otimes\text{s}\otimes\text{d}} * \epsilon_{\gamma} \quad (\text{C.9})$$

$$(\text{LiveTime})_{\text{b}\otimes\text{s}\otimes\text{d}} = \frac{N_{\text{b}\otimes\text{s}\otimes\text{d}}(\text{raw} - \text{data})}{N_{\text{b}\otimes\text{s}\otimes\text{d}}(\text{scaler})} \quad (\text{C.10})$$

- N_{γ} : number of the photon peaks
- $(\text{Livetime})_{\text{b}\otimes\text{s}\otimes\text{d}}$: live time for *BEAM* \otimes *SSD* \otimes *DALI* trigger
- ϵ_{γ} : efficiency of DALI

ϵ_{γ} was estimated by **GEANT**.

C.1.1 The list of trigger event and livetime

RUN	²⁶ Ne+Pb	²⁶ Ne+Al	²⁶ Ne+emp
Ungated Trigger(scaler)	14852201	4920463	1551938
Accepted Trigger(scaler)	13598070	4738277	152043
beam⊗SSD⊗DALI(scaler)	11084097	2136137	378380
beam⊗SSD⊗DALI(raw-data)	10038675	1952605	328419
beam⊗SSD⊗NEUT(scaler)	3306474	2166475	547899
beam⊗SSD⊗NEUT(raw-data)	2982517	1979953	472618
DS-Beam(scaler)	1578423	1755869	822505
DS-Beam(raw-data)	1443494	1630666	725995
Beam	789451741	878002704	411256850
Live Time(all)	0.92	0.96	0.98
Live Time(bsd)	0.91	0.91	0.87
Live Time(bsn)	0.90	0.91	0.86
Live Time(ds)	0.91	0.93	0.88
DS-factor	500	500	500
²⁶ Ne(raw-data)*(livetime)	501886813	553961828	272365909

Table C.1: The table of trigger event.

In $BEAM \otimes SSD \otimes NEUT$ trigger,

To subtract the empty target run to reject the background components in $BEAM \otimes SSD \otimes NEUT$ trigger, the statics of Al target run, and Pb target run is normalized by the empty run.

$$\langle \text{pureTarget} \rangle = C1 \langle \text{target} \rangle - C2 \langle \text{empty} \rangle \quad (\text{C.11})$$

Number of Pb run and Al and empty, respectively, scaled by the number of the incident beam after correcting livetime of the detector.

The Cross section table C.6 obtained from previous data is following.

Cross-section correcting to the acceptance of the SSD is the following.

RUN	$^{26}\text{Ne}+\text{Pb}(\text{live time})$	$^{26}\text{Ne}+\text{emp}(\text{live time})$	$^{26}\text{Ne}+\text{emp}(\text{live time})$
^{25}Ne	20772(22827)	12780(14044)	2372(2758)
^{24}Ne	41016(45073)	34830(38274)	7187(8357)
^{23}Ne	37059(40724)	33639(36965)	7500(8720)
^{22}Ne	46131(50693)	43195(47467)	9967(11589)
^{21}Ne	31151(34232)	21717(23865)	4691(5454)
^{20}Ne	2363 (2597)	3454(3796)	1427(1659)

Table C.2: In $BEAM \otimes SSD \otimes NEUT$ trigger, the number of Ne isotopes reaction products from A of 26 to A of 20 in coincidence with neutron threshold 5 MeV. Veto counters has no hit.

RUN	$^{26}\text{Ne}+\text{Pb}$	$^{26}\text{Ne}+\text{Al}$	$^{26}\text{Ne}+\text{empty}$
lifetime of the trigger	0.9	0.91	0.86
factor for incident beam	C1=0.603	C1=0.543	C3=1.163

Table C.3: The scaling factor for normalizing of run. Trigger is $BEAM \otimes SSD \otimes NEUT$.

RUN	$^{26}\text{Ne}+\text{Pb}(\text{error})$	$^{26}\text{Ne}+\text{Al}(\text{error})$
^{25}Ne	10557 (154)	4100(85)
^{24}Ne	17461 (165)	10197(141)
^{23}Ne	14416 (157)	9093(139)
^{22}Ne	17091 (176)	112211(157)
^{21}Ne	14299 (145)	6075(111)
^{21}Ne	-	46(44)

Table C.4: In $BEAM \otimes SSD \otimes NEUT$ trigger, The number of Ne isotopes reaction products from A of 26 to A of 20 after subtracting empty target run at Pb and Al target, respectively, in coincidence with neutron threshold 5 MeV. Veto counters has no hit.

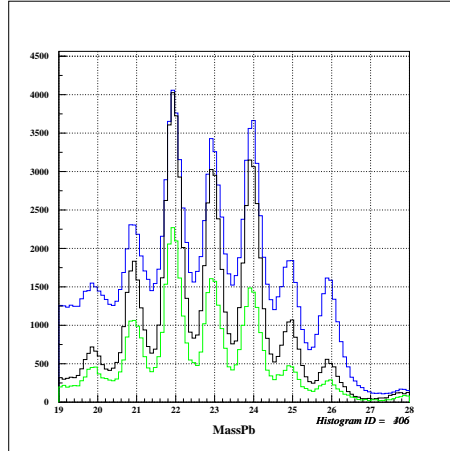


Figure C.1: The mass distribution of Ne isotopes on SSD at Pb target, Al and empty, respectively, without acceptance correction. The number of Pb and Al, respectively is scaled by a empty run. Blue line, black line and green line are mass distribution of Pb target run, Al and empty, respectively.

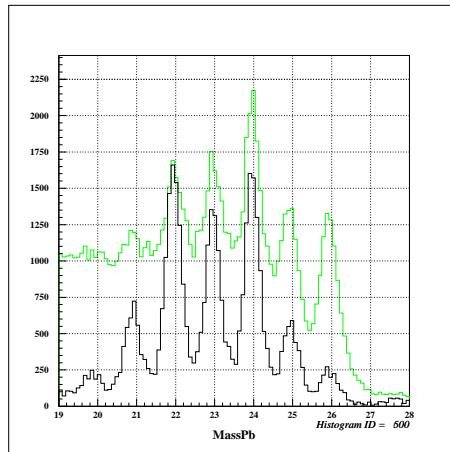


Figure C.2: The mass distribution of Ne isotopes on SSD at Pb target and Al target, respectively, after subtracting empty run without acceptance correction. The number of Pb and Al, respectively, is scaled by a empty run. The green line and black is Pb target run and Al, respectively.

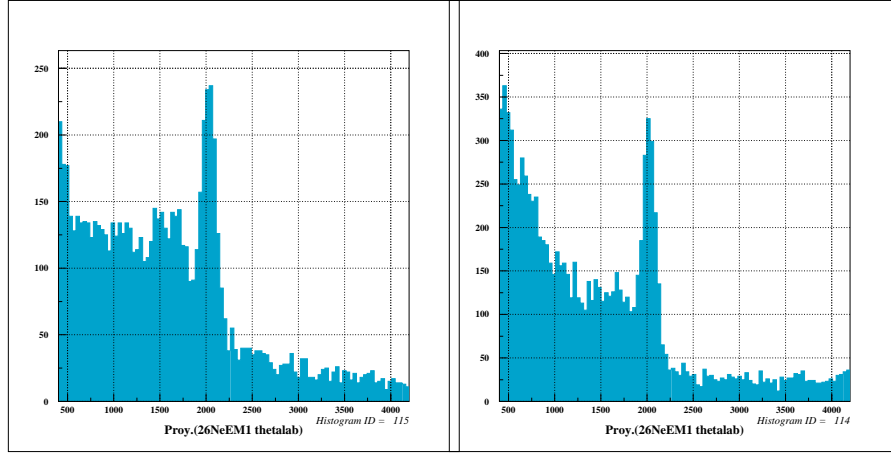


Figure C.3: The 26^+ peak of the ^{26}Ne at Al target. Figure C.4: The 26^+ peak of the ^{26}Ne at Pb target.

RUN	$^{26}\text{Ne}+\text{Pb}(\text{error})[\text{mb}]$	$^{26}\text{Ne}+\text{Al}(\text{error})[\text{mb}]$
^{25}Ne	58.0(0.9))	5.2(0.2)
^{24}Ne	95.9(1.3)	12.9(0.23)
^{23}Ne	79.2(1.3)	11.5(0.22)
^{22}Ne	93.9(1.7)	14.2(0.26)
^{21}Ne	78.6(2.9)	7.7(0.18)
^{20}Ne	-	0.1(0.15)

Table C.5: In $BEAM \otimes SSD \otimes NEUT$ trigger, the cross section of Ne isotopes reaction products from A of 26 to A of 20 after subtracting empty target run at Pb and Al target, respectively, in coincidence with neutron threshold 5 MeV. Veto counters has no hit. The acceptance correction of SSD was not performed. The acceptance and efficiency of neutron was not also performed.

RUN	$^{26}\text{Ne}+\text{Pb}(\text{error})[\text{mb}]$	$^{26}\text{Ne}+\text{Al}(\text{error})[\text{mb}]$
^{25}Ne	257(6)	18(0.7)
^{24}Ne	471(5.5)	43(1.1)
^{23}Ne	403(6.1)	30(1.6)
^{22}Ne	447(6.1)	37(1.6)

Table C.6: After correcting the acceptance of the SSD. In $BEAM \otimes SSD \otimes NEUT$ trigger, the cross section of Ne isotopes reaction products from A of 26 to A of 20 after subtracting empty target run at Pb and Al target, respectively, in coincidence with neutron threshold 5 MeV. Veto counters has no hit. The acceptance correction of SSD was not performed. The acceptance and efficiency of neutron was not also performed.

RUN	$^{26}\text{Ne}+\text{Pb}$	$^{26}\text{Ne}+\text{Al}$
photo-peak(before accept) $E(2020 \text{ keV}; 2^+)$	1236	844
photo-peak(after accept) $E(2020 \text{ keV}; 2^+)$	3101	3670
ϵ efficiency	13.6%	13.6%
$\Delta\epsilon/\epsilon$	20%	20%
ϵ acceptance	39.8%	31.1%
σ cross-section(mb) exp	75(15)	18.5(3.7)
σ cross-section(mb) previously[12]	74(13)	

Table C.7: The $E(2020; 2^+ \rightarrow \text{g.s.})$ cross section of the ^{26}Ne at Pb and Al target, respectively.

C.1.2 Error estimation of cross section

In this section, the way of the error estimation for cross section is shown in following.

$$\sigma_{\text{reaction}} = \frac{N_{\text{frag}}}{N_B} \frac{A}{tN_A} \quad (\text{C.12})$$

- σ_{reaction} : cross section
- N_{fragment} : number of the reaction products
- N_B : number of the incident beam
- $A[\text{g/mol}]$: mass number
- $t[\text{g/cm}^2]$: thickness of the target
- $N_A[1/\text{mol}]$: Avogadro number

The error $\Delta\sigma$ of the cross section is given by following.

$$\Delta\sigma = \sqrt{\left(\frac{\Delta N_{\text{frag}}}{N_{\text{frag}}}\right)^2 + \left(\frac{\Delta\epsilon_{\text{frag}}}{\epsilon_{\text{frag}}}\right)^2 + \left(\frac{\Delta N_B}{N_B}\right)^2} \quad (\text{C.13})$$

- ΔN_B : statics error of the incident beam
- ϵ : acceptance correction of SSD
- $\Delta\epsilon$: acceptance correction error of SSD
- $\Delta N_{\text{frag}}^{\text{sta}}$: statics error of the reaction products number
- $\Delta N_{\text{frag}}^{\text{fit}}$: fitting error of the reaction spectrum spectrum on SSD

Subtracting empty target run from Pb and Al target, respectively, run produce the error of the Pb and Al target run, respectively, with the error of the empty run.

In empty run, Δx is the error of the empty run.

$$N_{\text{emp}} = x \pm \Delta x \quad (\text{C.14})$$

In Pb and Al run, respectively, Δy is the error of the Pb and Al run, respectively.

$$N_{\text{tgt}} = y \pm \Delta y \quad (\text{C.15})$$

F is the number of the total event after subtracting the empty target run.

$$F = N_{\text{tgt}} - C1 * N_{\text{emp}} \quad (\text{C.16})$$

Therefore,

$$\Delta N_{\text{frag}} = \Delta F \quad (\text{C.17})$$

- C1: coefficient in normalizing target statics

$$\Delta F = \sqrt{\left(\frac{\delta F}{\delta x}\right)^2 (\Delta x)^2 + \left(\frac{\delta F}{\delta y}\right)^2 (\Delta y)^2} \quad (\text{C.18})$$

$$\frac{\delta F}{\delta x} = 1 \quad (\text{C.19})$$

$$\frac{\delta F}{\delta y} = C1 \quad (\text{C.20})$$

Therefore,

$$\Delta F = \sqrt{(\Delta x)^2 + (\Delta y * C1)^2} \quad (\text{C.21})$$

In the γ -ray spectrum case,

$$\sigma = \frac{N_{\gamma}}{N_{\text{beam}}} \frac{A}{tN_A} \quad (\text{C.22})$$

Therefore,

$$\frac{\Delta \sigma}{\sigma} = \sqrt{\left(\frac{\Delta N_{\gamma}}{N_{\gamma}}\right)^2 + \left(\frac{\Delta \epsilon_{\gamma}}{\epsilon_{\gamma}}\right)^2 + \left(\frac{\Delta N_B}{N_B}\right)^2} \quad (\text{C.23})$$

$$\Delta N_\gamma = \sqrt{(\Delta N_\gamma^{\text{sta}})^2 + (\Delta N_\gamma^{\text{fit}})^2} \quad (\text{C.24})$$

- σ : cross section
- N_γ : number of the photo-peak number
- ϵ : efficiency of the DALI
- N_B : statics error of the incident beam
- $\Delta N_\gamma^{\text{sta}}$: statics error of the photo-peak number
- $\Delta N_\gamma^{\text{fit}}$: fitting error of the photo-peak spectrum

D Gold Haber Model

$$\Delta = \sqrt{\frac{F(A-F)}{A-1}}\sigma_0 \quad (\text{D.1})$$

where

- A: mass number of the projectile
- F: mass number of the fragment
- $\sigma_0^2 = \frac{1}{5}P_F^2$
- Δ : momentum distribution of the fragment

$$\langle (\sum \mathbf{P}_i)^2 \rangle = \sum_{i=1} \langle \mathbf{P}_i^2 \rangle + \sum_{i \neq j} \langle \mathbf{P}_i \cdot \mathbf{P}_j \rangle = A \langle \mathbf{P}_i^2 \rangle + A(A-1) \langle \mathbf{P}_i \cdot \mathbf{P}_j \rangle = 0 \quad (\text{D.2})$$

$$\Delta^2 = \langle \mathbf{P}_F^2 \rangle = \langle \sum_{i=1}^F (\mathbf{P}_i)^2 \rangle = F \langle \mathbf{P}_i^2 \rangle + F(F-1) \langle \mathbf{P}_i \cdot \mathbf{P}_j \rangle \quad (\text{D.3})$$

$$\sqrt{\langle P_F^2 \rangle} = \sqrt{\frac{F(A-F)}{A-1}} \sqrt{\langle P_i^2 \rangle} = \frac{1}{5}P^2_0 \sqrt{\frac{F(A-F)}{A-1}} \simeq 90 \sqrt{\frac{F(A-F)}{A-1}} \text{MeV} \quad (\text{D.4})$$

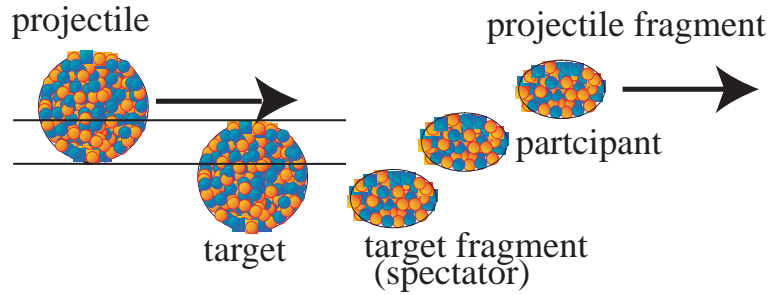


Figure D.1: Fragmentation

According to the model developed by Goldhaber[3], the width of the parallel momentum width σ in the fragment is the following.

$$\Delta = \sigma_0 \sqrt{\frac{F(A-F)}{A-1}} \sigma_0 = \frac{1}{5} P_F \quad (\text{D.5})$$

where

- F: mass number of the fragment
- A: mass number of the projectile
- Δ : the momentum distribution of the fragment
- P_F : Fermi momentum of nucleon

At relative energies, the momentum distribution of the projectile fragments are well described by Gaussian functions of the form.

$$\frac{d^3\sigma}{dP^3} = C \exp\left(-\frac{P_\perp}{2\sigma_\perp}\right) \exp\left(-\frac{(P_\parallel - P_0)^2}{2\sigma_\parallel^2}\right) \quad (\text{D.6})$$

where C is a normalization constant. The variables P_\perp and P_\parallel are the fragment momentum in the directions parallel and perpendicular to the beam respectively. The average fragment momentum in the beam direction is P_0 .

The angular distribution of the fragment in the laboratory frame is described in the following by the thesis[10]. The variance of the momentum distributions in the directions parallel and perpendicular to the beam are σ_\perp^2 and σ_\parallel^2 respectively.

Eq.D.6 can be transformed in the laboratory frame into the double differential cross section.

$$P = \sqrt{2A_F E_F} \quad (\text{D.7})$$

$$P_\parallel = P \cos \theta, \quad P_\perp = P \sin \theta \quad (\text{D.8})$$

$$\frac{d^2\sigma}{dE d\Omega} = N_0 (A_F, E_F)^{1/2} \exp\left(-A_F \left(\frac{E_F \sin^2 \theta}{\sigma_\perp} + \frac{E_F \cos^2 \theta - 2(E_F \bar{E})^{1/2} + \bar{E}}{\sigma_\parallel^2} \right)\right) \quad (\text{D.9})$$

where N_0 is a normalization coefficient, E_F its laboratory kinetic energy, \bar{E} its most probable kinetic energy and θ is the laboratory detection angle.

In the condition of the experiment, $\sigma_\parallel \simeq \text{constant}$, and $\sin \theta \simeq \theta$, $\cos \theta = 1$ for $\theta \simeq 0$.

$$\frac{d\sigma}{d\Omega} = C_1 \exp\left(-A_F \frac{E_F \theta^2}{2\sigma_\perp}\right) \quad (\text{D.10})$$

In the in the thesis[10], σ_0 is 87 MeV/c.

Therefore free parameter is σ_D .

$$\sigma_{\perp}^2 = \frac{A_F(A_P - A_F)}{A_P - 1} \sigma_0^2 + \frac{A_F(A_F - 1)}{A_P(A_P - 1)} \sigma_D^2 \quad (\text{D.11})$$

where

- A_P : projectile mass number
- A_F : fragment mass number
- σ_D : deflection of the projectile the nuclear and Coulomb fields of the target prior to fragmentation

D.1 Coulomb dissociation from the Cross-section

To investigate the narrow component, the cross section integrated over the angle in laboratory frame from 1 degrees to 5 degrees in the narrow component and wide component at Pb and Al targets were measured, respectively(see in Table. D.1 and D.2.)

Mass	Pb (wide)	Al(wide)
25	288.9(4.6)	273.3(30.5)
24	282.1(4.7)	273.9(9.2)
23	257.8(7.1)	265.6(7.8)
22	234.7(8.6)	268.0(3.6)

Table D.1: The cross section table for the wide component integrated over angle between 1 and 5 degrees at Pb and Al targets.

Mass	Pb (narrow)	Al Pb(narrow)
25	92.0(2.0)	133.5(14.3)
24	88.9(1.6)	122.5(7.7)
23	85.9(2.1)	119.6(17.1)
22	81.(1.9)	60.3(4.2)

Table D.2: The integrated cross section table for the narrow component integrated over angle between 1 and 5 degrees at Pb and Al targets.

By using these cross section of the narrow and wide components, respectively. the following possibilities were considered.

1. $\sigma_{\text{narrow}}/\sigma_{\text{wide}}$ decreases with the neutron for the fragment decrease.?

The energy of the excited states though Coulomb dissociation process is lower than that of the excited states though the nuclear breakup by the limited photon number(see in Fig. 2.4). Thus, the contribution of the Coulomb dissociation is probably decreases with the neutron of the fragment decrease. But this consideration was not enhanced at the Pb target (see in Fig.D.3).

2. The ratio $\sigma_{\text{narrow at Pb}}/\sigma_{\text{narrow at Al}}$ enhanced ($Z_{\text{Pb}}/Z_{\text{Al}}$) as simply model, amplitude of Rutherford scattering?

The narrow component is at the angle between 1 and 2.5 degrees and this component started from 0 degrees. Therefore, the integration for must be calculated from 0 degrees. To check precision of the integrated ratio from 0

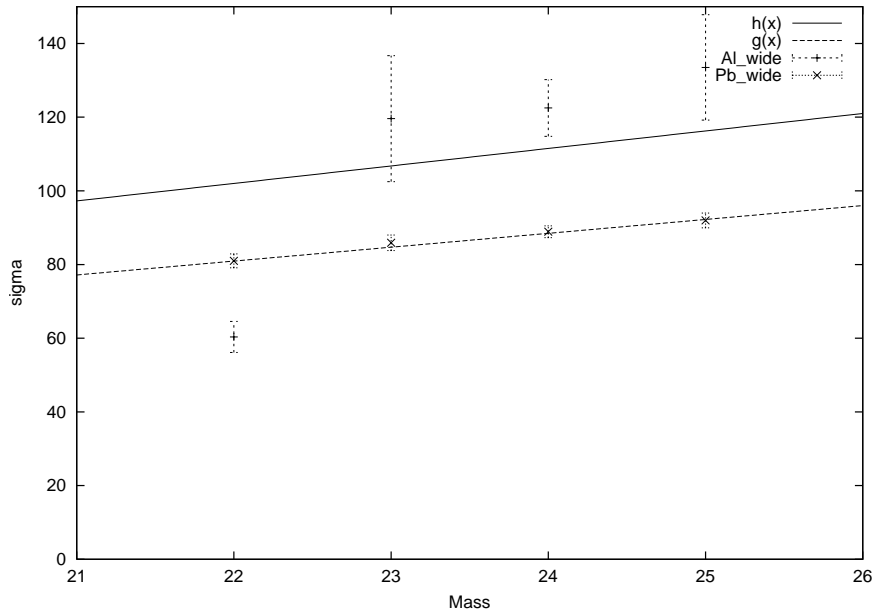


Figure D.2: The σ_{\perp} for the wide component. The solid line is not agreement with GoldHaber model calculation. In the assumption of $\sigma_0=0$, the deflection parameter of $\sigma_d = 96(0.3)$ and $121(15)$ was calculated at Pb and Al target, respectively.

degrees for extrapolation, firstly the ratio of wide component cross section was measured. These ratio was compared to the detected angle between 1 and 5 degrees. As a result, these ratio are agreement with each other in Fig. D.4. In the next step, the ratio of narrow component cross section was measured as same procedure. But the large ambiguity was shown in Fig. D.5.

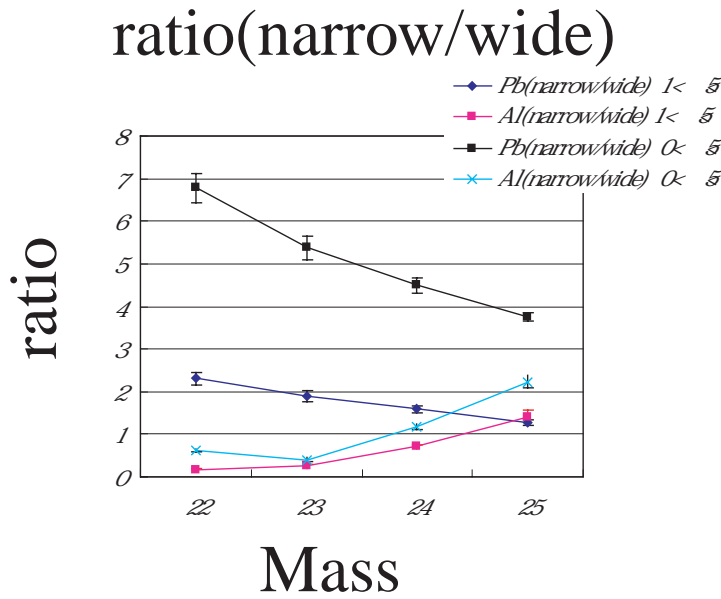


Figure D.3: The figure of the ratio, $\sigma_{\text{narrow}}/\sigma_{\text{wide}}$. This figure shows that the narrow component between Pb and Al target is symmetric tendency.

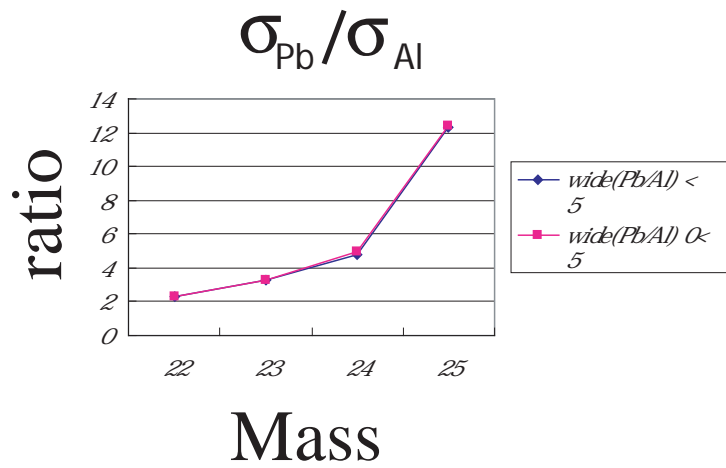


Figure D.4: The ratio of $\sigma_{\text{Pb}}/\sigma_{\text{Al}}$ for wide component at the laboratory region from 1 to 5 degree and extrapolation region from 0 to 5 degree. The ratio of two region is almost same and this shows that the extrapolation is adequacy.

ratio(Pb/Al) narrow parts

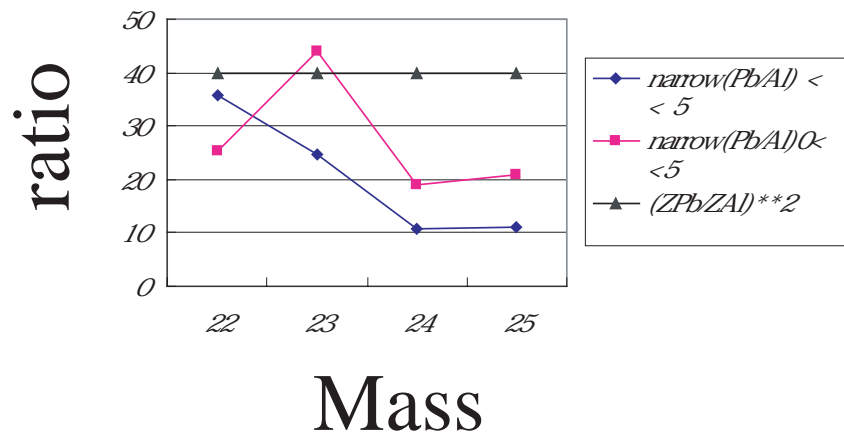


Figure D.5: The table of σ_{Pb}/σ_{Al} for narrow component between $A=22$ to $A=26$. This figure shows that the ratio of the laboratory frame from 1 degrees to 5 degrees and extrapolation frame from 0 degrees to 5 degrees is different from each other. This shows that the ambiguity of the forward angle. The black line is based on the assumption of the simple mode Rutherford scattering. This model is dependent on the charge of target, $\sigma \simeq Z^2_{tgt}$. In the thesis, the problem on the narrow component was not resolved.

E Acknowledgements

During the thesis work at the University of Tokyo Institute of Technology, I have had the so many privilege with many truly fine individuals. Firstly I give great thanks to my instructor, professor Nakamura for his support and encouragement.

I thank to the R332 collaborators in this experiment for taking good data. In the experiment, I thank these people for not only collaborating our experiment but also teaching me how to perform in the experiment. I thank to Julien in my collaborator of the experiment and analysis. The discussion with him helps me and the unique idea from him gives me many contribution. I express to Fukuda-san and Satoh-san for giving variety answer to my numerous questions on the experiment and physics.

A special acknowledgement goes to the people of Nakamura laboratory, Vinod-san, Sugimoto-san, Miura-san, Kondo-san, Matsui-san, Watanabe-san, Ohara-san, Nakabayashi-san, Hashimoto-san for discussing about so many problem.

Finally I would like to thank my parents, brother, ground mother, and friends for their continuous encouragement and supports.

Collaborators Special Thanks to Julien Gibelin ^B, Koichi Yoshida ^E, Takashi Nakamura ^A, Didier Beaumel ^B, Nori Aoi ^E, Hidetada Baba ^D, Yorick Blumenfeld ^B, Zoltan Elekes ^E, Naoki Fukuda ^E, Tomoko Gomi ^D, Yosuke Kondo ^A, Akito Saito ^D, Yoshiteru Sato ^A, Eri Takeshita ^D, Satoshi Takeuchi ^E, Takashi Teranishi ^C, Yasuhiro Togano ^D, Victor Lima ^B, Yoshiyuki Yanagisawa ^E, Attukalathil Mayyan Vinodkumar ^A, Toshiyuki Kubo ^E, Tohru Motobayashi ^E

A: Department of Physics, Tokyo Institute of Technology

B: Institut de Physique Nuclaire, Orsay, France

C: University of Tokyo (CNS), RIKEN Campus

D: Department of Physics, Rikkyo University

E: The Institute of Physical and Chemical Research (RIKEN)

Bibliography

- [1] I. Tanihata et al.: Phys. Rev. Lett **55**, 2676(1985).
- [2] T. Kobayashi et al.: Phys. Rev. Lett **60**, 2599(1988).
- [3] A.S. Goldhaber.: Phys. Rev. Lett. **B53**, 306(1974).
- [4] R. Anne et al.: Phys. Lett. **B250**, 19(1990).
- [5] N. A. Orr et al.: Phys. Rev. Lett. **69**, 2050(1992).
- [6] T. Nakamura et al.: Phys. Lett. **B331**, 296(1994).
- [7] R. Anne et al.: Nucl. Phys. **A575**, 125(1994).
- [8] N. A. Orr: Phys. Rev. Lett. **69**, 2050(1992).
- [9] T. Nakamura et al.: Phys. Rev. Lett **83**, 1112(1999).
- [10] R. Dayras et al.: Nucl. Phys. **A460**, 299(1986).
- [11] A. Leistenschneider et al.: Phys. Rev. Lett **86**, 24(2001).
- [12] B. V. Pritychenko et al.: Phys. Lett. **B461**, 322(2001).
- [13] T. Kubo et al.: Nucl. Instrum. Methods. **B70**, 309(1992).
- [14] H. Kumagai et al.: Nucl. Instrum. Methods. **A470**, 562(2001).
- [15] J.A. Winger et al.: Nucl. Instrum. Methods. **B70**, 380(1992).
- [16] S. Takeuchi et al.: RIKEN Accel. Prog. Rep. **36**, 148(2002).
- [17] K. Ikeda.: Nucl. Phys. **A538**, 355c(1992).
- [18] D.J. Horen et al.: Phys. Lett. **A99B**, 385(1981).
- [19] C.A. Bertulani et.al: Phys. Rep. **163**, 299(1988).
- [20] J.D. Jackson, Classical Electrodynamics 2nd Ed. (John Wiley & Sons, New York 1975).
- [21] O. Sorlin et al.: Nucl. phys. **A685**, 186c(2001)

- [22] A. Ozawa et al.: Nucl. phys. A**693**, 32(2001)
- [23] R. H. Stokes et al.: Rev. Sci. Instr **29**, 61(1958)
- [24] T. Nakamura: Doctor thesis, Tokyo University
- [25] K. Yoneda: Doctor thesis, Tokyo University
- [26] Z. Ma, private communication